Cytoskeletal-based mechanisms differently regulate in vivo and in vitro proplatelet formation

Alicia Bornert, Julie Boscher, Fabien Pertuy, Anita Eckly, David Stegner, Catherine Strassel, Christian Gachet, François Lanza, Catherine Leon

Published Ahead of Print on April 23, 2020, as doi:10.3324/haematol.2019.239111.

haematologica
Journal of The Ferrata Storti Foundation

Cytoskeletal-based mechanisms differently regulate *in vivo* and *in vitro* proplatelet formation

by Alicia Bornert, Julie Boscher, Fabien Pertuy, Anita Eckly, David Stegner, Catherine Strassel, Christian Gachet, François Lanza, and Catherine Léon

Haematologica 2020 [Epub ahead of print]

Citation: Alicia Bornert, Julie Boscher, Fabien Pertuy, Anita Eckly, David Stegner, Catherine Strassel, Christian Gachet, François Lanza, and Catherine Léon. Cytoskeletal-based mechanisms differently regulate in vivo and in vitro proplatelet formation.
Haematologica. 2020; 105:xxx
doi:10.3324/haematol.2019.239111

Cytoskeletal-based mechanisms differently regulate *in vivo* and *in vitro* proplatelet formation

Alicia Bornert[1], Julie Boscher[1], Fabien Pertuy[1], Anita Eckly[1], David Stegner[2], Catherine Strassel[1], Christian Gachet[1], François Lanza[1], Catherine Léon[1*]

[1] Université de Strasbourg, INSERM, EFS Grand Est, BPPS UMR-S 1255, F-67000 Strasbourg, France

[2] Institute of Experimental Biomedicine, University Hospital Würzburg & Rudolf Virchow Center for Experimental Biomedicine, University of Würzburg, 97080 Würzburg, Germany

Running heads: *In vivo* proplatelet formation

*Correspondence to: Catherine Léon, PhD
UMR_S1255 INSERM-Université de Strasbourg
Etablissement Français du Sang (EFS)
10, rue Spielmann, B.P. N°36
67065 Strasbourg Cedex, France
Tel: (33) 388 21 25 25
Fax: (33) 388 21 25 21
E-mail: catherine.leon@efs.sante.fr

Word counts : Abstract : 148
Main text : 4036
Number of Figures : 8
1 supplemental file and 8 videos associated

Abstract

Platelets are produced by bone marrow megakaryocytes through cytoplasmic protrusions, named native proplatelets (nPPT), into blood vessels. Proplatelets also refer to protrusions observed in megakaryocyte culture (cPPT*)* that are morphologically different. Contrary to cPPT, the mechanisms of nPPT formation are poorly understood. We show here in living mice that nPPT elongation is in equilibrium between protrusive and retraction forces mediated by myosin-IIA. We also found, using WT and β1-tubulin-deficient mice, that microtubule behavior differs between cPPT and nPPT, being absolutely required *in vitro*, while less critical *in vivo*. Remarkably, microtubule depolymerization in myosin-deficient mice did not affect nPPT elongation. We then calculated that blood Stokes' forces may be sufficient to promote nPPT extension, independently of myosin and microtubules. Together, we propose a new mechanism for nPPT extension that might explain contradictions between severely affected cPPT production and moderate platelet count defects in some patients and animal models.

Introduction

Blood platelets are key elements of hemostasis for the prevention of bleeding and are produced by a unique mechanism. They arise from megakaryocytes (MKs), specialized cells in the bone marrow[1, 2]. Upon differentiation from hematopoietic progenitors, MKs undergo endomitosis, leading to a giant cell, whose cytoplasm is filled by a highly developed intracellular membrane network called the demarcation membrane system (DMS)[3]. At a mature stage, MKs lie adjacent to the bone marrow sinusoid vessels and initiate cytoplasmic protrusion through the vessel wall. These protrusions further elongate inside the blood circulation, attached to their mother cells. These extensions are named proplatelets (PPTs) and are fueled by the DMS that acts as a membrane reservoir to allow PPT growth[4]. Once inside the blood stream, PPTs are released into the circulation as large fragments that have been proposed to further remodel in downstream organs to release *bona fide* platelets, small anucleated MK fragments having a discoid shape[2, 5, 6].

The first PPT term was proposed following *in situ* scanning electron microscopy (SEM) of "long intrasinusoidal "proplatelet" processes which originate from the cell body of extravascularly located megakaryocytes"[7]. Later on, *in vivo* observations by time lapse imaging in living animal confirmed the morphology of PPTs as elongated protrusions in WT mice under physiological conditions[7-14]. The same denomination was also given to the cytoplasmic MK extensions in culture or in bone marrow explants[8, 15-19]. Yet, the morphology of PPTs observed *in vitro* strongly differs from that observed *in situ*/*in vivo*. Early *in vitro* observations of marrow explants[8, 15, 16, 20] and later of progenitor-differentiated MKs in culture[17, 19, 21] similarly recorded PPTs presenting branched thin shafts (1-4 µm in diameter) leading to an entanglement of PPTs surrounding the MKs body[17-19]. These morphological differences between these two types of MK extensions raise the possibility that the mechanisms at stake could as well differ between *in vitro* cultured PPTs (hereafter referred as cPPT) and *in vivo* generated native PPTs (referred as nPPT).

While the mechanisms governing cPPT extension *in vitro* have been well documented, no study has really evaluated the *in vivo* cytoskeleton-based mechanisms regulating the extension of nPPT. Based on *in vitro* experiments, several cytoskeletal elements have been identified as playing a major role[22, 23].

Inside cPPTs, the microtubules are organized as linear bundles of mixed polarity running along the shaft and ending as a coil in the cPPT bud, prefiguring the platelet marginal band[2, 17, 24]. Incubating MKs *in vitro* in the presence of microtubule depolymerizing drugs prevented *de novo* cPPT extension[17, 21, 25, 26] and retracted already formed cPPT[16, 17, 21]. More recent work suggests that the sliding property of microtubules, rather than their proper polymerization, is the primary driver of cPPT extension[11, 24]. On the other hand, actin has been proposed to play a role in the branching process since F-actin depolymerization reduces the number of bifurcations[17], while myosin activity rather decreases the extension of cPPT and has no impact on their morphology except on the bud size[26, 27].

In the present study we examined whether the mechanisms previously described *in vitro* also apply to the nPPT by genetically and pharmacologically manipulating cytoskeletal key components. We show that in the bone marrow of living mice, the mechanism governing nPPT extension differs from the previously one described *in vitro*.

Methods

See detailed methods in Supplemental file

This study was approved by the local ethical committee and agreements for experimentation obtained from the French government (Agreement numbers: 2016090911005304 and 2018061211274514).

Intravital imaging

Intravital imaging was performed with either *mT/mG;Pf4-cre* mice[28] or following MKs and PPT staining by intravenous injection of an AF488-conjugated anti-GPIX antibody derivative[29]. Two photon microscopy was performed by observation of skull bone marrow as described[29]. Anesthetized mice where observed for a maximum of 3h, during which time one to four PPTs could be recorded.

In vitro proplatelet formation.

Bone marrow experiments were performed as described[26]. *In vitro* liquid culture of Lin^- mouse progenitors was performed as described previously[30].

Immunofluorescence and confocal observations

For *in situ* immunolabeling of bone marrow, we took care to preserve the cytoskeleton and immunolabeling was performed on 30 µm-thick sections unless otherwise stated.

Results

Distinct morphologies between *in vivo* PPTs (nPPTs) and *in vitro* cultured PPTs (cPPTs).

As already shown by others[4, 7, 9, 10, 31, 32], nPPTs extending into bone marrow sinusoids are unbranched and elongated processes that appears mostly as fragments larger than cPPT. This can be observed *in situ* in fixed tissue by GPIbβ immunolabeling or SEM (Fig. 1Ai-iii, see also Fig. 4C), clearly showing the slightly bulbous aspect of their ends (Fig. 1A, ii and iii inset). As also previously shown by others, two-photon microscopy observation in living animal confirmed this elongated morphology, sometimes irregular with constriction zones, which can be observed over long distances (Fig. 1Bi-iii and Videos 1-3 and Suppl. Fig.S1A). nPPTs were rarely found to segment at their extremities, but rather broke off as long fragments that will need to further remodel into individual platelets (Suppl. Fig. S1B).

In contrast, the morphology of cPPT appears highly different. Using different microscopy techniques, cPPTs observed *in vitro*, either from cultured MKs or cultured marrow explants, present a regular thin shaft terminated by a bud (Fig. 1Ci-iii). cPPTs shaft diameter is 4 times smaller than the shafts measured on nPPTs (Fig. 1D), notwithstanding the different microscopy techniques used for their observations. The cPPT bud diameter was found to be twice in size as the cPPT shaft (Fig. 1D, left panel). Furthermore, the cPPT buds are already discoid especially visible by scanning electron microscopy (SEM) (Fig. 1Cii, arrows), prefiguring the future platelet, contrary the nPPT ends (Fig. 1Aii-iii).

These data that essentially confirm previous observations by others are presented for comparison purposes as these important PPT morphological differences between *in vitro* and *in vivo* observations suggest that the underlying mechanisms might be different. We therefore evaluated the role of the cytoskeleton in the dynamics of nPPT formation.

In vivo nPPT elongation dynamics is regulated by myosin IIA that opposes driving forces.

As observed *in vivo* by two-photon microscopy, nPPT elongation is a dynamic and irregular process which proceeds through elongation periods interspersed with pause and retraction phases as

exemplified in Fig. 2A (red and blue traces) (see also Suppl. Fig. S2B for more tracings), resulting in high variability in elongation speed (Suppl. Fig. S2A). We hypothesized that this irregular behavior resulted from opposing forces exerted by the cytoskeleton and that the myosin contractile cytoskeleton was a likely contributor. We previously showed that *Myh9*$^{-/-}$ mice had a quantitative defect in cPPT formation in the explant marrow model, with fewer MKs extending PPTs that were also less complex compared to the WT[26]. Here using intravital microscopy, we were nevertheless able to find *Myh9*$^{-/-}$ extensions within sinusoids (Fig. 2B). However, in contrast to WT nPPTs, myosin-deficient cytoplasmic processes elongation occurred without any pause or retraction phases as exemplified in Fig. 2C (Suppl. Fig. S2C). Furthermore, the elongation speed was twice as high as that of the WT, which might be explained by the absence of pauses and retractions (Fig. 2D). Interestingly, they were longer and thinner (Fig. 2). Their mean length was increased by 49 % in *Myh9*$^{-/-}$ as compared to WT PPTs and the shafts were 28% thinner. These findings suggest that myosin IIA, by increasing intracellular tension, renders the cytoplasmic extensions less stretchable and participates in the pauses and retractions observed under normal conditions.

β1-tubulin deficiency prevents proplatelet formation *in vitro* but not *in vivo*.

Among other key cytoskeletal elements, microtubules have been shown to play the essential role in the dynamics of cPPT. To determine its role *in vivo*, we turned to mice deficient in β1 tubulin, the major beta tubulin isoform in platelets. MKs from *Tubb1*$^{-/-}$ mice were unable to extend protrusions *in vitro* in a bone marrow explant assay (Fig. 3A upper panel) and only rare abnormally short and compact extensions were observed following *in vitro* differentiation of bone marrow progenitors (Fig. 3A, lower panel inset), confirming previous results in fetal liver-derived MKs[33].

In situ, examining the *Tubb1*$^{-/-}$ bone marrow by immunolabeling, we found that the number of MK was increased by around 75% compared to the WT mice (Suppl. Fig. S3A), probably as a compensatory response to the thrombocytopenia (Suppl. Fig. S3B). *Tubb1*$^{-/-}$ mouse MKs were able to extend protrusions in marrow sinusoids, although we found a 45% decrease in the number of nPPT extensions compared to the WT, in agreement with the decreased number of circulating platelets (Fig.

3B and S3B). *Tubb1*$^{-/-}$ nPPTs exhibited a fully normal morphology (Fig. 3C) with a surprisingly normal elongation speed (Fig. 3D) and a fully normal mean length and width (Fig. 3E-F). These results indicate that while the absence of an essential tubulin isoform almost totally abrogate PPT formation *in vitro*, it partially affects the number of PPTs *in vivo* but not the elongation speed. Overall, this points to different mechanisms contributing to PPT extension when considering the *in vivo* situation with a less crucial importance of microtubules compared to *in vitro*.

Microtubules are non-uniformly distributed in proplatelets *in vivo*

Another difference between *in vivo* and *in vitro* was observed by looking at the cytoplasmic distribution of microtubules. Within cPPT obtained *in vitro*, microtubules are organized into a bundle running along the shaft as previously described[17] and as illustrated in Figure 4A. We then explored their organization *in situ* under conditions that preserved microtubules as denoted by the intact marginal band of platelets and mitotic spindles in marrow cells (see on Fig. 4C yellow arrowheads and arrows). As shown in Fig. 4B (left, arrowhead), microtubules were not organized as bundles but aligned roughly parallel in the direction of the extension in nascent nPPT. This different microtubule organization suggests a different role in the process of PPT extension. Of note, strong F-actin labelling was observed laterally at the site of transmigration, indicating also the importance of this cytoskeleton in this first step (Fig. 4B, middle). Focusing on later stages in the elongated nPPTs, we observed that again, unlike *in vitro*, the microtubules were not arranged in a large bundles running along the extension, and microtubules were not longitudinally aligned in parallel but rather in various orientations (Fig. 4B arrow and Fig. 4C-E; especially compare Fig. 4Aii with 4B and 4C having the same scale). A second observation was their non-uniform distribution all along the nPPT. As seen in Figure 4C showing a 3D view of 3 portions of intertwined nPPTs, the labelling was not always constant, being sometimes decreased (Fig. 4C left, orange arrowhead) or even absent (Fig. 4C left, orange arrow), suggesting few microtubules and mainly non-polymerized tubulin. Hence the difference for the importance of microtubules in the process of MK extension between *in vivo* and *in*

vitro is further illustrated by the difference in microtubule organization/distribution within nascent and elongating nPPTs compared to cPPT.

Administration of vincristine leads to shrinkage of preexisting WT proplatelets.

In a second approach, and because *Tubb1*$^{-/-}$ mice compensate the β1 tubulin deficiency by overexpressing β2 and β5 tubulin isotypes[33], we pharmacologically depolymerized microtubules within pre-formed nPPT. Microtubule depolymerization was induced during the course of nPPT elongation by injecting the microtubule-destabilizing drug vincristine in WT mice (1 mg/kg). At this dose, vincristine induces depolymerization of microtubules from the marginal band of circulating platelets and from marrow cells in the extravascular compartment (Suppl. Fig. S4 and S5). Time-lapse recordings showed that the majority of pre-formed nPPT underwent shrinkage within 10 min after vincristine administration as illustrated in Fig. 5A and Video 4, and quantified in Fig. 5B-D. Most nPPTs progressively became shorter (Fig. 5A-C) and increased their thickness, especially at their base (Fig. 5D). In some cases, the shrank fragments were seen being released into the circulation. Doubling the vincristine dose (2 mg/kg) accelerated PPT shrinkage as early as 2 minutes after drug administration (Fig. 5E). These results indicate that the microtubule cytoskeleton is required to maintain the nPPT elongated morphology once it is formed.

Microtubules are dispensable for *Myh9*$^{-/-}$ proplatelet elongation

Given that myosin IIA is required for the retraction phases observed in WT nPPTs, we investigated whether the shrinkage observed after injection of vincristine was dependent on myosin contractility. Again, we previously controlled that microtubules from *Myh9*$^{-/-}$ mouse platelets and MKs were sensitive to vincristine-induced depolymerization (Suppl. Fig. S4 and S5). Strikingly, no PPT shrinkage occurred after vincristine administration in *Myh9*$^{-/-}$ *mice*, rather the protrusions continued to elongate so rapidly that they often disappeared from the observation field before 10 min (video 5 and

Suppl. Fig. S6). Increasing vincristine dose to 2 mg/kg did not modify this surprising behavior, as again none of the *Myh9*$^{-/-}$ protrusions retracted, and elongation was continued (Fig. 6A-C).

Examination of the bone marrow sections by IF microscopy showed that *Myh9-/-* PPTs, like their WT counterparts, do not present a unique microtubule bundle (Suppl. Fig. S7, to be compared to Fig. 4D-E). Treatment with vincristine did not prevent the observation of long GPIbβ-positive protrusions despite no visible microtubules (Fig. 6D, arrow). These data indicate that the shrinkage following microtubule depolymerization is dependent on active myosin IIA.

Altogether these data show that in the absence of myosin IIA, microtubules were totally dispensable for nPPT elongation, indicating that elongation can be promoted by other driving forces, independently of microtubules.

Stokes' forces can contribute to PPT elongation.

Driving forces contributing to the elongation process could originate from blood flow. This hypothesis was initially supported by the observation that cessation of blood flow induced the relaxation of already preformed 3 nPTTs that extended in the same flow line (Fig. 7A and video 6), showing that blood flow maintains nPPT under tension.

Flows in sinusoids are complex due to the intricate anastomosis of the vasculature (Fig. 7B). This was evidenced by the monitoring of platelet movements inside vessels of living mice as in some cases, we observed areas of inverse flows (Fig. 7C and video 7). In these areas, PPTs were tossed from one branch of a vessel to another, without detaching (Fig. 7D and video 8). Since they remain attached to the stationary MKs in the bone marrow, PPTs are submitted to fluid force of the flowing blood all along their shafts and buds. Assuming the nPPT end as a sphere, the force can be calculated using the Stokes' formula $F=6\pi\eta LV$ where L is the radius of the sphere, V the velocity of the fluid and η the viscosity. The Stokes' force applied to the nPPT end was estimated based on the displacement of circulating platelets, recorded in vessels where nPPT were extended (V=213 µm/s (range 24-488) (Fig. 7E). The nPPT end having a mean radius of 4 µm (L) and the apparent viscosity η of the blood in

microvessels varying from 2 to $4x10^{-3}$ Pa.s[34-36], the Stokes' force approximates 30-60 pN on the bud. This can be considered as the minimal force as the Stokes' forces also apply all along the nPPT shaft. It is known from the literature that a force around 20-50 pN is usually required to extend membrane nanotubes in cells including blood cells such as neutrophils or erythrocytes[37-39]. Hence the forces exerted by the blood flow on the whole nPPT would be high enough to substantially contribute to nPPT extension.

Discussion

In this study we evaluated the mechanisms of nPPT formation as it occurs *in vivo* inside bone marrow sinusoid vessels. We found that they differ from those taking place for cPPTs produced under *in vitro* conditions, especially with regards to the relative implication of two main cytoskeletal components, *i.e.* microtubules and myosin.

We show that the non-continuous nPPT elongation process resulting from pause and retraction phases resulted from myosin IIA. MKs are known to activate myosin IIA in response to local increase in shear [40, 41]. Blood flow within sinusoid vessels present heterogeneous shear stresses ranging from null to 10 dyn/cm[2, 42, 43] generating forces that are sufficient to trigger cellular mechanotransduction in endothelial cells[44]. Hence, depending on the flow forces, transient myosin activation could increase membrane tension to preserve its integrity. Conversely, a decreased myosin IIA activity would increase membrane compliance and stretching, promoting thinner and longer protrusions such as observed in *Myh9*$^{-/-}$ mice. Another hypothesis could be that myosin-promoted pauses serve to slow down extension so that DMS properly enter the nPPT. In favor of this hypothesis, we observed *in situ* that myosin-deficient nPPTs contain very few DMS membranes compared to WT ones (Suppl. Fig. S8), which could also explain the thinner aspect of these *Myh9*$^{-/-}$ nPPT.

Unexpectedly, the microtubule behavior was found to differ between nPPTs and cPPTs. This was first revealed in *Tubb1*$^{-/-}$ mice *in vivo*. Although the number of MK extending nPPT was decreased, in agreement with the moderate thrombocytopenia, their morphology and elongation speed

were fully normal. This was in stark contrast to the almost total inability of *Tubb1*$^{-/-}$ MK to form cPPTs *in vitro.* These findings are a further indication that the defects of *Tubb1*$^{-/-}$ mice are exacerbated *in vitro* and a clear evidence of mechanistic differences between the two environments.

Given these observations, we hypothesize that MK extensions generated *in vivo* are less dependent on microtubules than anticipated from cPPT produced *in vitro*. We observed that microtubules were present in the nascent nPPT, although not organized in bundles, as also previously mentioned in earlier work[8]. Their presence however suggested that they might still play a role in nPPT initiation, in agreement with the decreased number of *Tubb1*$^{-/-}$ nPPT observed *in situ*. *In vivo*, the precise intracellular mechanisms controlling the initiation and transmural passage of nPPTs are still unknown. The first step of nPPT extension, which initiates in the marrow stroma and in absence of blood forces, might require higher protrusive forces to push against the endothelial barrier compared to the liquid culture. It is most probable that both F-actin and microtubule cytoskeletons jointly play a role as we also observed strong F-actin accumulation in MKs at the site where the nascent nPPT cross the vessel wall (Fig. 4B). This F-actin accumulated in structures resembling sort of shoulders which could correspond to the fibrillary-rich collars previously observed by Behnke & Forer and could be an anchorage point for facilitating the initial protrusion[31;4]. At this stage, whether microtubules directly contribute together with F-actin to promote the initial pushing force for transmural passage, or whether they are indirectly required to organize vesicles/organelles transport to bring essential components or play a role as information carriers for F-actin is not known[45].

Upon subsequent nPPT growth inside sinusoids, we observed a non-uniform distribution of microtubules inside elongated nPPT which clearly differs from the microtubule bundles uniformly lining the cPPT shafts and ending as coils observed *in vitro*. Although we were beyond the resolution limit to see microtubule arrangement in areas of strongest nPPT constriction *in situ*, these were clearly observed as unbundled in larger areas, in agreement with early observations by Behnke mentioning random arrangement in large clumps of MK cytoplasm released in sinusoids *in situ*[8]. Radley and Scurfield also observed *in situ* that microtubules were aligned in constriction zones but splayed out on either side of the constriction[46]. These results confirm and extend those recently published by Brown

et al. showing by tomography that *in situ*, microtubules were individual and randomly distributed in MK protrusions[4]. Hence all the above data point to a different mechanism depending on whether MK extend protrusions *in vitro* or *in vivo*. However, microtubules are clearly important for maintaining the elongated nPPT structure in WT mice. This was evidenced here after inducing *in vivo* microtubule depolymerization on pre-existing nPPT.

A much unexpected observation in *Myh9*$^{-/-}$ mice was the continuous growth of MK protrusions within sinusoids even when microtubules were depolymerized by vincristine. This indicated that under conditions where contractile forces are weakened, abrogating nPPT retraction, elongation of protrusions is still occurring. Hence, inside the blood vessels, microtubules would be less crucial for nPPT elongation. Isolated microtubules have a low pushing force in the range of 3-4 pN, while it has been demonstrated that organization in bundles increases their force-generating capacity in an additive fashion[47-49]. While *in vitro* microtubule bundles could conceivably be the primary driving force for elongation, this is different *in vivo* where the essential role of microtubules would be to act as a backbone to transport constituents and to prevent and counteract myosin-mediated nPPT retraction. Of note, *Tubb1*$^{-/-}$ platelets do not present abnormalities in their granule distribution (see Suppl. Fig. S3C) contrary to knockout mice having actomyosin impairments[32, 50], showing that partial microtubule content is sufficient to promote normal organelle transport into the maturing MK and the nPPT.

Our finding then raised the question of the force promoting MK fragment elongation *in vivo*. Our data suggest that the main motor for nPPT elongation may come from hemodynamic forces. The importance of blood flow was previously noted by data showing increased cPPT elongation velocity under flow compared to static conditions[11, 51], and from our observations that nPPTs always align in the direction of flow, especially visible upon inverse flows (video 8) or when flow stopped (video 6) (Fig. 7). Even with low blood flow velocities as in sinusoids, ranging from about ten to several hundred µm/s[42, 43] (Fig. 7E), we calculated that the Stokes' force exerted on the nPPT end would be sufficient to stretch the membrane[37-39]. The same forces, applied all along the PPT shaft, would further increase the overall driving force and promote its extension. Taking into account the fact that DMS fuses with plasma membrane all along the nPPT shaft as shown by Brown et al.[4], this continuous

membrane replenishment most probably considerably decreases membrane tension as demonstrated in other systems[52, 53], thus lowering even more the forces required for nPPT elongation.

Our findings do not exclude a key role of microtubules in the final platelet formation. We may speculate that this final nPPT remodeling into barbell platelets and final platelets could occur through microtubule-based mechanisms, similar to those previously established in liquid culture[6, 11], leading to microtubule coils prefiguring the marginal band. In favor of this idea, Lefrançais *et al*. recently published videos of free MK fragment remodeling in lung vessels that produced extensions strikingly resembling branched cPPTs extended by MKs in culture[5] . In addition, we could observe *in situ* barbell platelets and free nPPT fragments having microtubule organization similar to cPPT including microtubules coils (personal observation and [54]).

From the present work added to early data, it seems clear that the cytoplasmic processes of MKs are structurally different *in vivo* and *in vitro* due to the different mechanisms leading to their extension. The question then arises as to the respective nomenclature of these extensions. Should the term PPT be used for extensions within the bone marrow or for the extensions observed in *in vitro* systems, or even for MK fragments released into the circulation and which are truly "pro"-platelets? Defining distinct nomenclatures for each of these structures might help to get a clearer picture of thrombopoiesis in pathophysiology compared to the *in vitro* platelet production process. We propose that the large MK fragments extended *in vivo* are named "nPPTs" for native PPTs, opposing to "cPPT" (for cultured PPTs) present *in vitro*.

We therefore propose a model for the nPPT formation in the bone marrow that differs from the one established *in vitro*. *In vivo*, while microtubules may contribute to the initial cytoplasmic extension of the nascent nPPT, they appear to be far less important for the elongation process once the nPPT inside the blood flow. Microtubules rather play a role as a backbone to prevent nPPT retraction mediated by actomyosin contraction. nPPT elongation per se could proceed through blood drag forces that stretch nPPT plasma membrane as it is fueled by the DMS. We propose that this *in vivo* mechanism which occurs in the native and complex marrow environment, is bypassed in the liquid culture conditions. The *in vitro* microtubule-based mechanisms previously described should take place in a second time,

once the nPPTs has been freed inside the blood circulation (Fig. 8). Taken together, these data may explain why in some cases, strong discrepancies were observed between the capacity to extend cPPT, quantified *in vitro*, compared to the moderately decreased circulating platelet count[33, 55, 56]. Our work may thus help to understand the mechanisms of thrombocytopenia in patients especially when mutations occur in cytoskeletal proteins.

Acknowledgements

AB was supported by a fellowship from EFS (APR2016). JB was a recipient of a FRM (foundation pour la Recherche Médicale) fellowship. The authors would like to thank Florian Gaertner (IST, Austria) for his expert advice on two-photon microscopy experiments and Yves Lutz at the Imaging Center IGBMC (Illkirch, France) for his expertise and help with the two-photon microscope. We thank Josiane Weber for excellent technical help and Jean-Yves Rinkel for help in 3D reconstructions. We thank Ramesh Shivdasani for his generous gift of *Tubb1*$^{-/-}$ mice. We thank Juliette Mulvihill for reviewing the English of the manuscript. We thank ARMESA (Association de Recherche et Développement en Médecine et Santé Publique) for support in the acquisition of the two-photon microscope.

Conflict-of-interest disclosure: The authors declare no competing financial interests.

References

1. Kaushansky K. Thrombopoiesis. Semin Hematol. 2015;52(1):4-11.

2. Machlus KR, Thon JN, Italiano JE Jr. Interpreting the developmental dance of the megakaryocyte: a review of the cellular and molecular processes mediating platelet formation. Br J Haematol. 2014;165(2):227-236.

3. Eckly A, Heijnen H, Pertuy F, et al. Biogenesis of the demarcation membrane system (DMS) in megakaryocytes. Blood. 2014;123(6):921-930.

4. Brown E, Carlin LM, Lo Celso C, Poole AW. Multiple membrane extrusion sites drive

megakaryocytes migration into bone marrow blood vessels. Life Sci Alliance. 2018;1(2):1-12.

5. Lefrancais E, Ortiz-Munoz G, Caudrillier A, et al. The lung is a site of platelet biogenesis and a reservoir for haematopoietic progenitors. Nature. 2017;544(7648):105-109.

6. Thon JN, Italiano JE Jr. Does size matter in platelet production? Blood. 2012;120(8):1552-1561.

7. Becker RP, De Bruyn PP. The transmural passage of blood cells into myeloid sinusoids and the entry of platelets into the sinusoidal circulation; a scanning electron microscopic investigation. Am J Anat. 1976;145(2):183-205.

8. Behnke O. An electron microscope study of the rat megacaryocyte. II. Some aspects of platelet release and microtubules. J Ultratruct Res. 1969;26(1):111-129.

9. Junt T, Schulze H, Chen Z, et al. Dynamic visualization of thrombopoiesis within bone marrow. Science. 2007;317(5845):1767-1770.

10. Kowata S, Isogai S, Murai K, et al. Platelet demand modulates the type of intravascular protrusion of megakaryocytes in bone marrow. Thromb Haemost. 2014;112(4):743-756.

11. Bender M, Thon JN, Ehrlicher AJ, et al. Microtubule sliding drives proplatelet elongation and is dependent on cytoplasmic dynein. Blood. 2015;125(5):860-868.

12. Nishimura S, Nagasaki M, Kunishima S, et al. IL-1alpha induces thrombopoiesis through megakaryocyte rupture in response to acute platelet needs. J Cell Biol. 2015;209(3):453-466.

13. Zhang L, Orban M, Lorenz M, et al. A novel role of sphingosine 1-phosphate receptor S1pr1 in mouse thrombopoiesis. J Exp Med. 2012;209(12):2165-2181.

14. Zhang L, Urtz N, Gaertner F, et al. Sphingosine kinase 2 (Sphk2) regulates platelet biogenesis by providing intracellular sphingosine 1-phosphate (S1P). Blood. 2013;122(5):791-802.

15. Leven RM, Yee MK. Megakaryocyte morphogenesis stimulated in vitro by whole and partially fractionated thrombocytopenic plasma: a model system for the study of platelet formation. Blood. 1987;69(4):1046-1052.

16. Radley JM, Haller CJ. The demarcation membrane system of the megakaryocyte: a misnomer? Blood. 1982;60(1):213-219.

17. Italiano JE, Jr., Lecine P, Shivdasani RA, Hartwig JH. Blood platelets are assembled principally at the ends of proplatelet processes produced by differentiated megakaryocytes. J Cell Biol. 1999;147(6):1299-1312.

18. Eckly A, Strassel C, Cazenave JP, Lanza F, Leon C, Gachet C. Characterization of megakaryocyte development in the native bone marrow environment. Methods Mol Biol. 2012;788:175-192.

19. Pouli D, Tozzi L, Alonzo CA, et al. Label free monitoring of megakaryocytic development and proplatelet formation in vitro. Biomed Opt Express. 2017;8(10):4742-4755.

20. Thiery JP, Bessis M. [Genesis of blood platelets from the megakaryocytes in living cells.]. C R Hebd Seances Acad Sci. 1956;242(2):290-292.

21. Tablin F, Castro M, Leven RM. Blood platelet formation in vitro. The role of the cytoskeleton in megakaryocyte fragmentation. J Cell Sci. 1990;97(Pt 1):59-70.

22. Ghalloussi D, Dhenge A, Bergmeier W. New insights into cytoskeletal remodeling during platelet production. J Throm Haemost. 2019;17(9).

23. Poulter NS, Thomas SG. Cytoskeletal regulation of platelet formation: Coordination of F-actin and microtubules. Tint J Biochem Cell Biol. 2015;66:69-74.

24. Patel SR, Richardson JL, Schulze H, et al. Differential roles of microtubule assembly and sliding in proplatelet formation by megakaryocytes. Blood. 2005;106(13):4076-4085.

25. Handagama PJ, Feldman BF, Jain NC, Farver TB, Kono CS. In vitro platelet release by rat megakaryocytes: effect of metabolic inhibitors and cytoskeletal disrupting agents. Am J Vet Res. 1987;48(7):1142-1146.

26. Eckly A, Rinckel JY, Laeuffer P, et al. Proplatelet formation deficit and megakaryocyte death contribute to thrombocytopenia in Myh9 knockout mice. J Thromb Haemost. 2010;8(10):2243-2251.

27. Eckly A, Strassel C, Freund M, et al. Abnormal megakaryocyte morphology and proplatelet formation in mice with megakaryocyte-restricted MYH9 inactivation. Blood. 2009;113(14):3182-3189.

28. Pertuy F, Aguilar A, Strassel C, et al. Broader expression of the mouse platelet factor 4-cre transgene beyond the megakaryocyte lineage. J Thromb Haemost. 2015;13(1):115-125.

29. Stegner D, vanEeuwijk JMM, Angay O, et al. Thrombopoiesis is spatially regulated by the bone marrow vasculature. Nat Commun. 2017;8(1):127.

30. Strassel C, Eckly A, Leon C, et al. Hirudin and heparin enable efficient megakaryocyte differentiation of mouse bone marrow progenitors. Exp Cell Res. 2012;318(1):25-32.

31. Behnke O, Forer A. From megakaryocytes to platelets: platelet morphogenesis takes place in the bloodstream. Eur J Haematol Suppl 1998;61:3-23.

32. Pertuy F, Eckly A, Weber J, et al. Myosin IIA is critical for organelle distribution and F-actin organization in megakaryocytes and platelets. Blood. 2014;123(8):1261-1269.

33. Schwer HD, Lecine P, Tiwari S, Italiano JE Jr., Hartwig JH, Shivdasani RA. A lineage-restricted and divergent beta-tubulin isoform is essential for the biogenesis, structure and function of blood platelets. Curr Biol. 2001;11(8):579-586.

34. Popel AS, Johnson PC. Microcirculation and Hemorheology. Ann Rev Fluid Mech. 2005;37:43-69.

35. Pries AR, Secomb TW. Microvascular blood viscosity in vivo and the endothelial surface layer. Am J Physiol Heart Circ Physiol. 2005; 289(6):H2657-2664.

36. Lipowsky HH. Microvascular rheology and hemodynamics. Microcirculation. 2005;12(1):5-15.

37. Borghi N, Brochard-Wyart F. Tether extrusion from red blood cells: integral proteins unbinding from cytoskeleton. Biophys J. 2007;93(4):1369-1379.

38. Hochmuth RM, Marcus WD. Membrane tethers formed from blood cells with available area and determination of their adhesion energy. Biophys J. 2002;82(6):2964-2969.

39. Shao JY, Hochmuth RM. Micropipette suction for measuring piconewton forces of adhesion and tether formation from neutrophil membranes. Biophys J. 1996;71(5):2892-2901.

40. Shin JW, Swift J, Spinler KR, Discher DE. Myosin-II inhibition and soft 2D matrix maximize multinucleation and cellular projections typical of platelet-producing megakaryocytes. Proc Natl Acad Sci U S A. 2011;108(28):11458-11463.

41. Spinler KR, Shin JW, Lambert MP, Discher DE. Myosin-II repression favors pre/proplatelets but shear activation generates platelets and fails in macrothrombocytopenia. Blood. 2015;125(3):525-533.

42. Bixel MG, Kusumbe AP, Ramasamy SK, et al. Flow Dynamics and HSPC Homing in Bone Marrow Microvessels. Cell Rep. 2017;18(7):1804-1816.

43. Mazo IB, von Andrian UH. Adhesion and homing of blood-borne cells in bone marrow microvessels. J Leukoc Biol. 1999;66(1):25-32.

44. Chao Y, Ye P, Zhu L, et al. Low shear stress induces endothelial reactive oxygen species via the AT1R/eNOS/NO pathway. J Cell Physiol. 2018;233(2):1384-1395.

45. Dent EW, Baas PW. Microtubules in neurons as information carriers. J Neurochem. 2014;129(2):235-239.

46. Radley JM, Scurfield G. The mechanism of platelet release. Blood. 1980;56(6):996-999.

47. Dogterom M, Yurke B. Measurement of the force-velocity relation for growing microtubules. Science. 1997;278(5339):856-860.

48. Kolomeisky AB, Fisher ME. Force-velocity relation for growing microtubules. Biophys J. 2001;80(1):149-154.

49. Vleugel M, Kok M, Dogterom M. Understanding force-generating microtubule systems through in vitro reconstitution. Cell Adh Migr. 2016;10(5):475-494.

through in vitro reconstitution. Cell Adh Migr. 2016;10(5):475-494.

50. Bender M, Eckly A, Hartwig JH, et al. ADF/n-cofilin-dependent actin turnover determines platelet formation and sizing. Blood. 2010;116(10):1767-1775.

51. Dunois-Larde C, Capron C, Fichelson S, Bauer T, Cramer-Borde E, Baruch D. Exposure of human megakaryocytes to high shear rates accelerates platelet production. Blood. 2009;114(9):1875-1883.

52. Gauthier NC, Masters TA, Sheetz MP. Mechanical feedback between membrane tension and dynamics. Trends Cell Biol. 2012;22(10):527-535.

53. Wang G, Galli T. Reciprocal link between cell biomechanics and exocytosis. Traffic. 2018;19(10):741-749.

54. Thon JN, Italiano JE. Platelet formation. Semin Hematol. 2010;47(3):220-226.

55. Strassel C, Eckly A, Leon C, et al. Intrinsic impaired proplatelet formation and microtubule coil assembly of megakaryocytes in a mouse model of Bernard-Soulier syndrome. Haematologica. 2009;94(6):800-810.

56. Strassel C, Magiera MM, Dupuis A, et al. An essential role for alpha4A-tubulin in platelet biogenesis. Life Sci Alliance. 2019;2(1):e201900309.

Legends to Figures

Figure 1. Proplatelets generated in the bone marrow *in vivo* (nPPT) are morphologically different from cultured PPT (cPPT). A) Representative images of *in situ* bone marrow nPPTs: GPIbβ immunolabeling and confocal observation of a 30 µm-thick bone marrow section showing a portion of a long nPPT extending from the mother MK (*) (i), and detail of a bulbous nPPT end (ii); images are 3D rendering using LASX software. (iii), several elongated nPPTs (arrows) observed in a sinusoid vessel by SEM. Inset, magnification showing a bulbous nPPT end. Note the various nPPT shaft widths. Representative of at least 3 mice. B) *In vivo* nPPTs: z-projection images from time-lapse experiments showing the various morphologies of nPPTs (arrows) extending within BM sinusoids. nPPTs and MKs are in green, sinusoid vessels are in red. Representative of at least 20 mice. C) Representative images *of in vitro* cPPTs: cPPTs produced by MKs differentiated in culture from mouse bone marrow progenitors, visualized by bright field microscopy at the bottom of the culture well before fixation (i) or after PFA-fixation and SEM observation (ii); (iii), cPPTs extending *in vitro* from a bone marrow explant, observed by phase contrast microscopy. D) Scatter plot representing cPPT shaft and terminal bud widths from explant BM measured on phase contrast images (left) (30-50 cPPT per group, data pooled from 2 individual marrow explants) or nPPT shaft and terminal bud widths from *in vivo* recordings (right). Mean±sem from 18 to 28 values, pooled from 14 mice. Statistics analyzed using Mann-Whitney comparison test.

Figure 2. Myosin regulates nPPT elongation speed. A) Normalized nPPTs length (%) of 3 independent WT mouse plotted over time, showing regular elongation (black line, max length = 282.1 µm), pauses between elongation phases (blue line, max length = 151.2 µm) or pause and retraction phases between elongation phases (red line, max length = 85.6 µm). Representative of nPPT from at least 10 WT mice. B) Two Z-projection images showing long, thin nPPTs in *Myh9*$^{-/-}$ bone marrow sinusoids (arrows). Dotted lines represent the contours of the sinusoids. Scale bar = 20 µm. Representative of at least 10 *Myh9*$^{-/-}$ mice. C) Normalized length (%) of 4 representative *Myh9*$^{-/-}$

nPPTs observed in 3 mice plotted over time, showing a continuous elongation, without pause or retraction (black line, max length = 175.1 µm; green line, max length = 221.2 µm; red line, max length = 132.7 µm; blue line, max length = 98.5 µm). D) nPPT elongation speed. Data are 12 nPPTs pooled from eight WT mice and 12 nPPTs pooled from 5 *Myh9*$^{-/-}$. E) nPPT length. Data are 25 nPPTs from 14 WT mice) and 13 nPPTs from 5 *Myh9*$^{-/-}$ mice. F) nPPT width close to the base of PPT. Data are 28 nPPTs from 19 WT mice and 17 nPPTs from 8 *Myh9*$^{-/-}$ mice. D-F, bar graphs represent the mean ± sem; p values were calculated using Mann-Whitney test.

Figure 3. Strong discrepancy between *in vitro* cPPT and *in vivo* nPPT formation in *Tubb1*$^{-/-}$ mice. A) Upper panel, explant bone marrow culture experiment. Representative phase contrast images and quantification of the % of MK presenting with cPPTs after 6-hours culture showing total absence of *Tubb1*$^{-/-}$ MK with protrusions (0%) while 55% of WT MKs extended cPPTs (mean±sem, n=3 independent experiments). Lower panel, MK forming PPTs after 4 days of Lin^{-} progenitor culture. Representative bright field images and quantification of the % of MK presenting with cPPTs (mean±sem, n=4 independent experiments). Inset, rare *Tubb1*$^{-/-}$ MK forming abnormal cPPTs without shaft extensions. B) Estimation of the nPPT formation capacity *in situ* by calculating the ratio of PPT fragments over the total number of MK observed in 30-µm thick marrow sections. Bars are mean ± sem of 3-4 independent marrow sections from 2 mice, representing 374 and 687 MKs for WT and *Tubb1*$^{-/-}$, respectively. C) Two z-projection images of *in vivo Tubb1*$^{-/-}$ nPPTs. Dotted lines delimit the sinusoids. Representative of at least 12 nPPTs from 5 mice. D) nPPT elongation speed. Data are mean ± sem of 16 nPPTs pooled from 8 WT mice and 12 nPPTs pooled from 4 *Tubb1*$^{-/-}$ mice. E) nPPT length. Data are mean ± sem of 25 nPPTs pooled from 14 WT mice and 16 nPPTs pooled from 5 *Tubb1*$^{-/-}$ mice. F) nPPT width. Data are mean ± sem of 28 nPPTs pooled from 19 WT mice and 16 nPPTs pooled from 5 *Tubb1*$^{-/-}$ mice. Bar graphs represent the mean ± sem; all data analyzed sing Mann-Whitney test. ns, not significant.

Figure 4. Microtubules are differentially distributed along PPTs *in situ* compared to *in vitro*. A) *i-ii*: cPPTs from WT MKs differentiated in culture for 4 days, labeled with an antibody against α tubulin. *iii:* microtubule bundles within the cPPT shaft and coils in the bud (inset), observed by SEM after removal of the membrane by treatment with Triton X-100. B) Confocal images of a nascent nPPT within bone marrow 30-µm thick sections revealing an absence of microtubule bundle organization (antibodies against α tubulin in green) and F-actin (phalloidin labeling, in magenta). Dotted lines represent sinusoid vessel. Note the presence of an nPPT transversally sectioned (arrow) in the sinusoid, again lacking microtubule bundles. C-E) *In situ* bone marrow nPPT immunolabeling with antibodies against α tubulin (green) and GPIbβ (magenta). C) 3D visualization of z-stack (30 µm thick) showing parts of 3 entangled PPTs after GPIbβ labeling, denoted PPT_1, PPT_2 and PPT_3. Tubulin labeling was discontinuous being weak to absent in certain portions of the nPPTs. For example, labeling becomes weaker in the upper part of the longest nPPT (PPT_3) (orange arrowhead). Tubulin labeling in the thinnest nPPT (PPT_2) was hardly visible in our settings (orange arrow). Marginal band of platelets (yellow arrowheads) and mitotic spindles (yellow arrows) were well labeled denoting well-preserved microtubules. D-E) Confocal single-plane images at higher magnification showing nPPT portions. Note that the microtubules are not arranged longitudinally. B-E), representative of 4 WT femur marrows from 2 mice.

Figure 5. : Vincristine infusion leads to shrinkage of preformed WT nPPTs. A) Representative z-projection time-lapse images showing an nPPT before and after vincristine administration (1 mg/kg). B) Length of individual nPPTs plotted as a function of time before and after 1 mg/kg vincristine administration. Seven mice analyzed. C) Scatter plot of nPPT length difference during a 10-minute observation showing elongation in the absence of vincristine and retraction following vincristine injection (from 0.5 to 10.5 min). Seven mice analyzed for each condition. D) Measurement of the difference in width close to the base during a 10-minute window showing small positive or negative variation in the absence of vincristine (left) and increasing width following vincristine injection

(right). Seven mice analyzed. E) Doubling the vincristine dose administration accelerates nPPT shrinkage. Seven mice analyzed. All data analyzed using Mann-Whitney test. ns, not significant.

Figure 6. *Myh9*$^{-/-}$ nPPT still elongate after vincristine administration. A) Representative z-projection time-lapse images showing *Myh9*$^{-/-}$ protrusions before and after vincristine administration. B) Measurement of protrusions length in *Myh9*$^{-/-}$ mice before and after 2 mg/kg vincristine administration plotted as a function of time. Note that some *Myh9*$^{-/-}$ protrusions could not be recorded after 4.5 min since they escaped the observation field. Six mice analyzed. C) Measurement of the difference in length during a 4-min window (0.5 – 4.5 min post 2 mg/kg vincristine injection), showing retraction in WT mice and elongation in *Myh9*$^{-/-}$ mice. Seven WT mice and 6 *Myh9*$^{-/-}$ mice analyzed, using Mann-Whitney statistical analysis. D) Immunolabeling of bone marrow sections from *Myh9*$^{-/-}$ mice injected with vincristine (1 mg/kg) 10 min before removal of the femurs and fixation of the bone marrow, showing the absence of microtubule labeling in a long protrusion (arrow). Left, Magenta labeling showing GPIbβ; center, green labeling showing α tubulin; images represent a 3D view. Right panel, 3D representation of the MK extending the nPPT obtained by image segmentation and 3D reconstruction with AMIRA software.

Figure 7. PPTs are under the influence of blood flow. A) z-projection time-lapse images showing relaxation of 3 nPPT after cessation of blood flow due to cardiac arrest of the mouse, revealing the presence of 3 nPPTs (indicated by the white, yellow and blue arrows). Observed in 3 mice. B) z-projection showing the anastomosis of the sinusoid vessels in the skull bone marrow. Arrows indicate the flow direction illustrating the complexity of the flows in sinusoids. C) Detail of a sinusoid bifurcation leading to inverse flows (opposed red and blue arrows). The flow velocity in each portion of the vessel as a function of time is plotted on the graph (red line, left side; blue line, right side), showing phases of stasis, accelerations and decelerations. D) Time-lapse images of an nPPT in the same bifurcation as in C, oscillating according to the flow direction. E) Graph showing the platelet

velocities measured in vessels where nPPTs were recorded (mean±SEM, 9 mice). Note the large variations.

Figure 8. The proposed model depicting the cytoskeletal-based differences between *in vivo* and *in vitro* PPT formation.

In cPPTs generated *in vitro*, initiation and elongation depend entirely on the microtubule cytoskeleton organized as linear bundles along the PPT shafts and ending as a coil (1), already prefiguring the marginal band of the future platelets, while F-actin would promote branching. *In vivo*, the initiation of nPPT formation takes place in the marrow and depends on both actin and microtubule cytoskeletons (2). During nPPT elongation in the sinusoid circulation, microtubules do not form a unique bundle but are mostly isolated and play a critical role to counteract myosin-based nPPT retraction (3), while drag forces contribute to the protrusive forces. The released elongated nPPT fragments will further remodel in the downstream microcirculation to give the final circulating platelets, possibly through microtubule-based mechanisms similar to *in vitro* (4).

Figure 1.

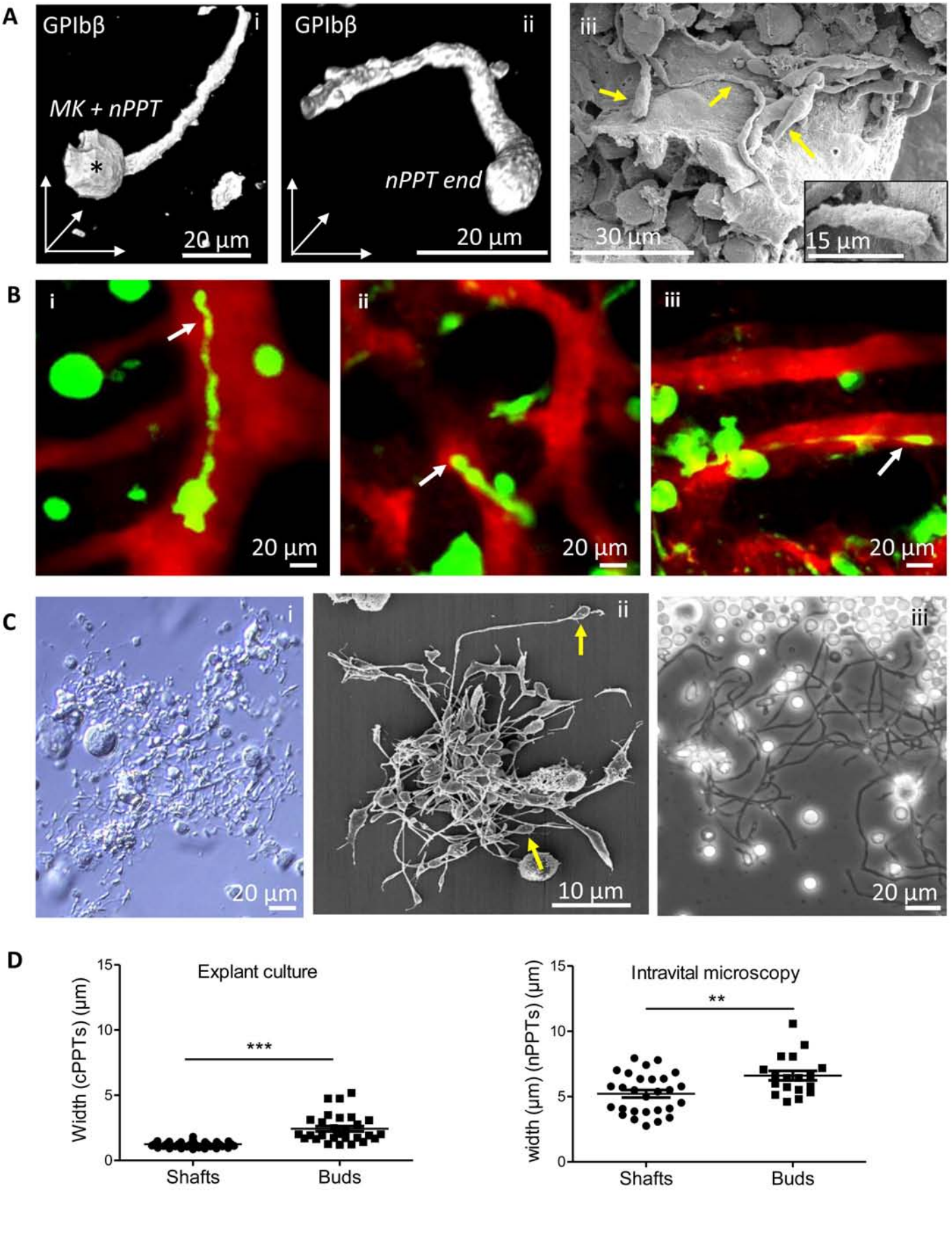
A
GPIbβ
i
MK + nPPT
*
20 µm
GPIbβ
ii
nPPT end
20 µm
iii
30 µm
15 µm
B
i
20 µm
ii
20 µm
iii
20 µm
C
i
20 µm
ii
10 µm
iii
20 µm
D
Explant culture
Width (cPPTs) (µm)
15
10
5
0
***
Shafts
Buds
Intravital microscopy
width (µm) (nPPTs) (µm)
15
10
5
0
**
Shafts
Buds

Figure 2.

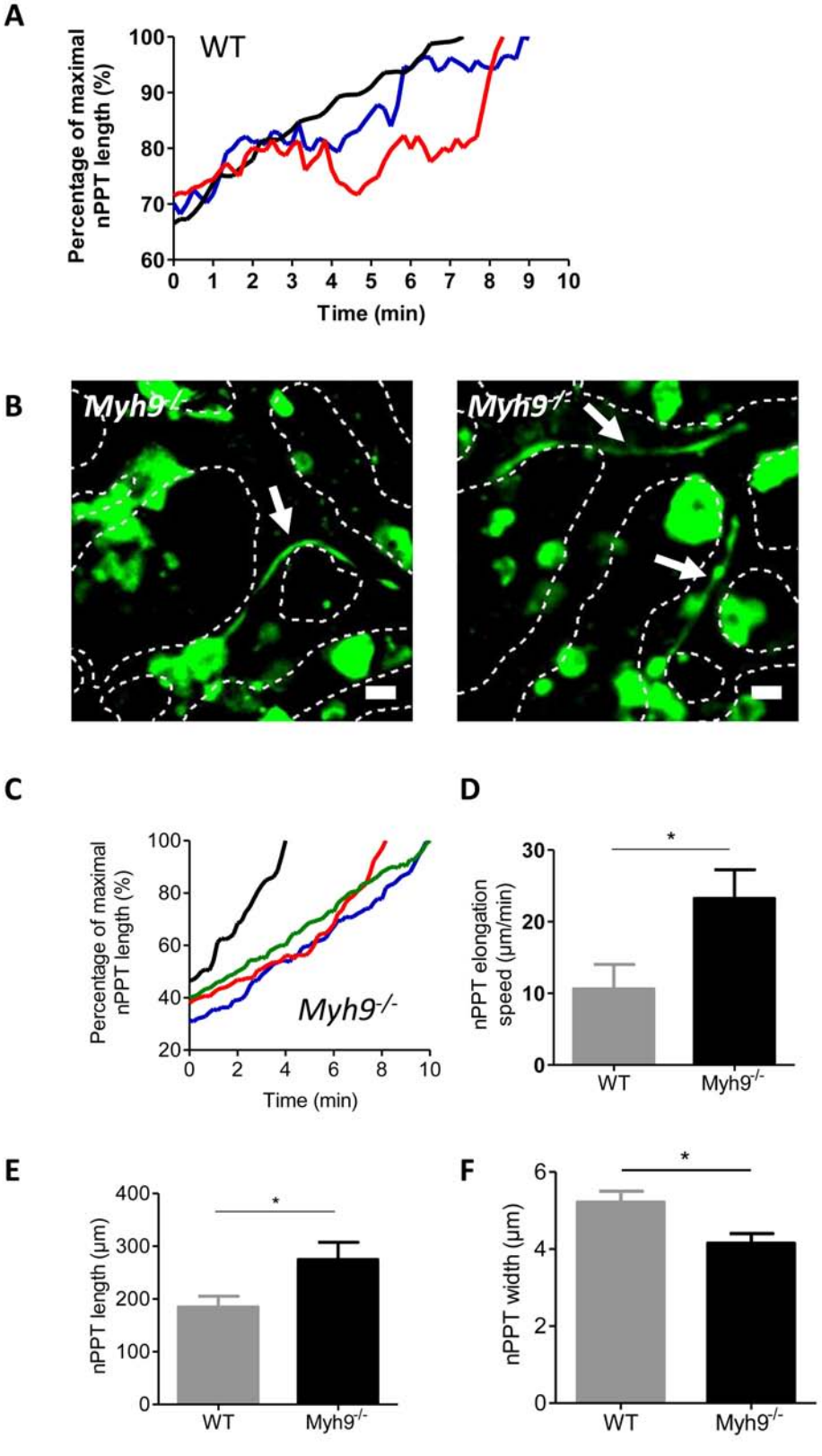
A
WT
Percentage of maximal nPPT length (%)
Time (min)
B
Myh9-/-
Myh9-/-
C
Myh9-/-
Percentage of maximal nPPT length (%)
Time (min)
D
nPPT elongation speed (μm/min)
WT
Myh9-/-
E
nPPT length (μm)
WT
Myh9-/-
F
nPPT width (μm)
WT
Myh9-/-

Figure 3.

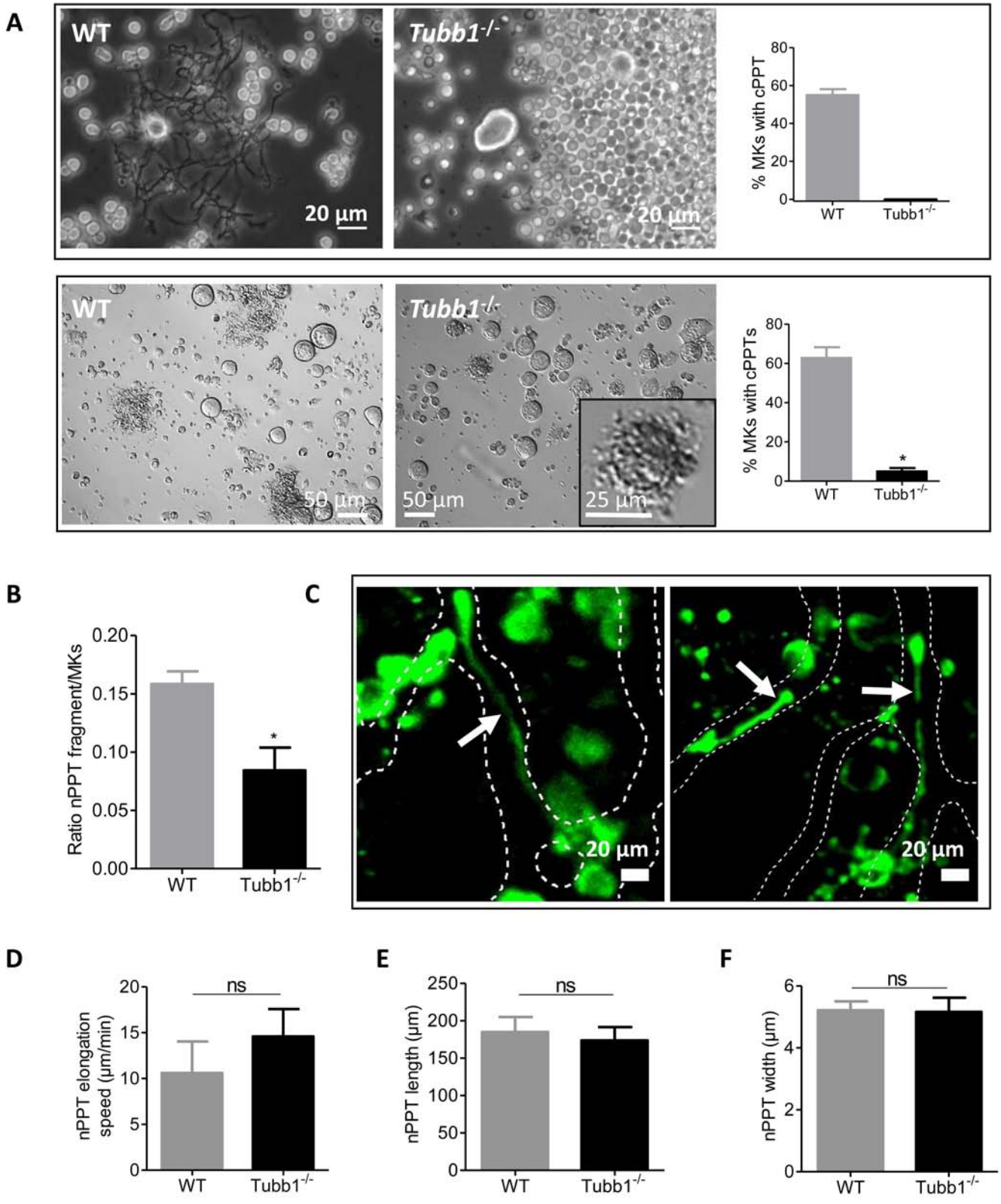
A
WT
Tubb1-/-
20 µm
20 µm
% MKs with cPPT
80
60
40
20
0
WT
Tubb1-/-
WT
Tubb1-/-
50 µm
50 µm
25 µm
% MKs with cPPTs
80
60
40
20
0
*
WT
Tubb1-/-
B
Ratio nPPT fragment/MKs
0.20
0.15
0.10
0.05
0.00
*
WT
Tubb1-/-
C
20 µm
20 µm
D
nPPT elongation speed (µm/min)
20
15
10
5
0
ns
WT
Tubb1-/-
E
nPPT length (µm)
250
200
150
100
50
0
ns
WT
Tubb1-/-
F
nPPT width (µm)
6
4
2
0
ns
WT
Tubb1-/-

Figure 4.

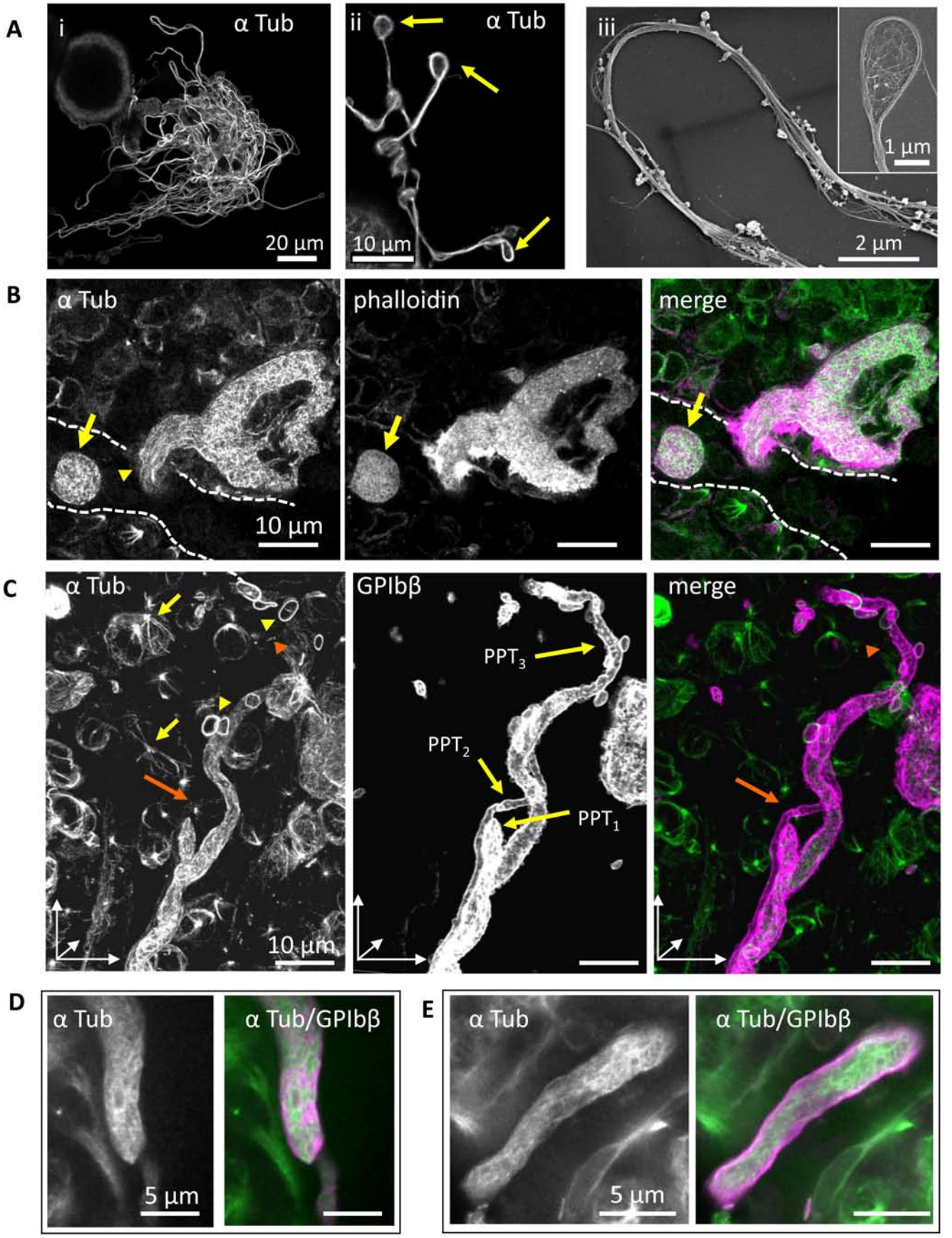
A
i
α Tub
20 μm
ii
α Tub
10 μm
iii
1 μm
2 μm
B
α Tub
10 μm
phalloidin
merge
C
α Tub
10 μm
GPIbβ
PPT3
PPT2
PPT1
merge
D
α Tub
5 μm
α Tub/GPIbβ
E
α Tub
5 μm
α Tub/GPIbβ

Figure 5.

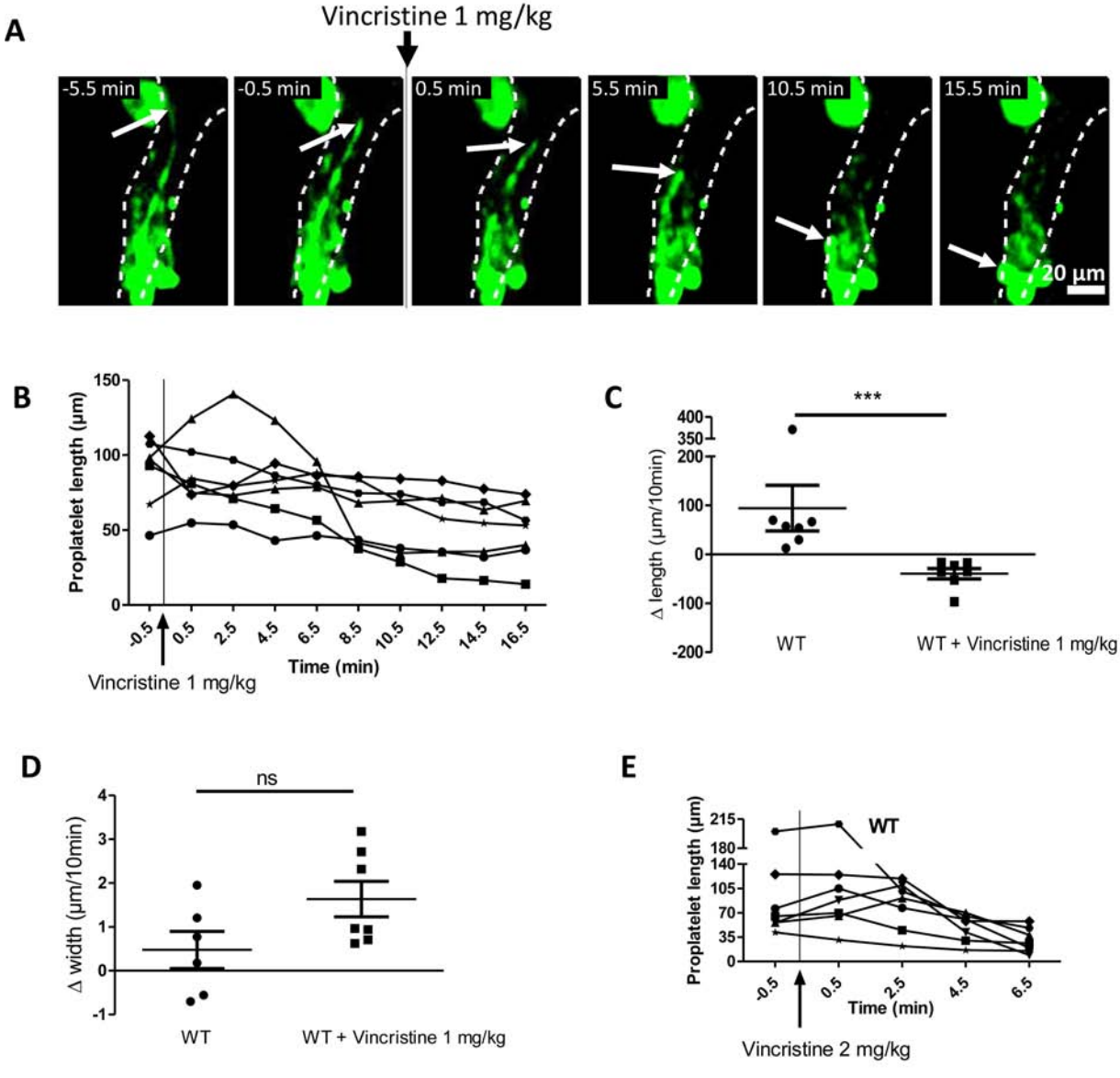
A
Vincristine 1 mg/kg
-5.5 min
-0.5 min
0.5 min
5.5 min
10.5 min
15.5 min
20 µm
B
Proplatelet length (µm)
150
100
50
0
-0.5
0.5
2.5
4.5
6.5
8.5
10.5
12.5
14.5
16.5
Time (min)
Vincristine 1 mg/kg
C
***
Δ length (µm/10min)
400
350
200
100
0
-100
-200
WT
WT + Vincristine 1 mg/kg
D
ns
Δ width (µm/10min)
4
3
2
1
0
-1
WT
WT + Vincristine 1 mg/kg
E
Proplatelet length (µm)
215
180
140
105
70
35
0
WT
-0.5
0.5
2.5
4.5
6.5
Time (min)
Vincristine 2 mg/kg

Figure 6.

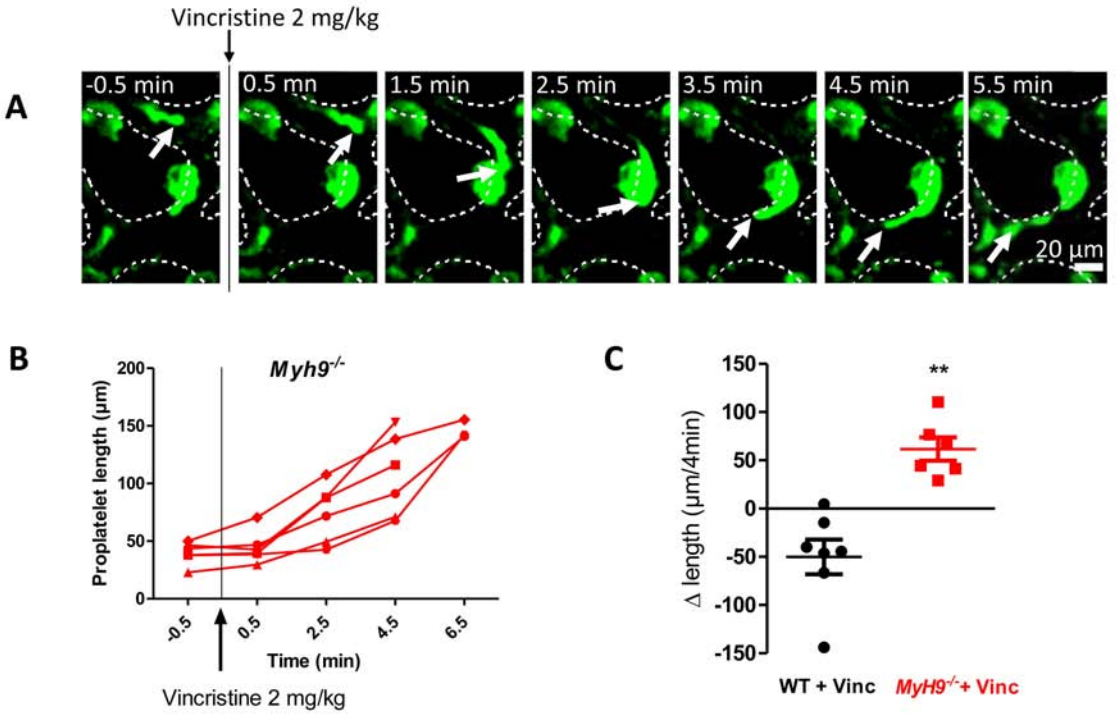
A
Vincristine 2 mg/kg
-0.5 min
0.5 mn
1.5 min
2.5 min
3.5 min
4.5 min
5.5 min
20 µm
B
Myh9-/-
Proplatelet length (µm)
200
150
100
50
0
-0.5
0.5
2.5
4.5
6.5
Time (min)
Vincristine 2 mg/kg
C
Δ length (µm/4min)
150
100
50
0
-50
-100
-150
**
WT + Vinc
MyH9-/- + Vinc
D
GPIbβ
Tubulin
Image segmentation
y (µm)
x (µm)
z (µm)

Figure 7.

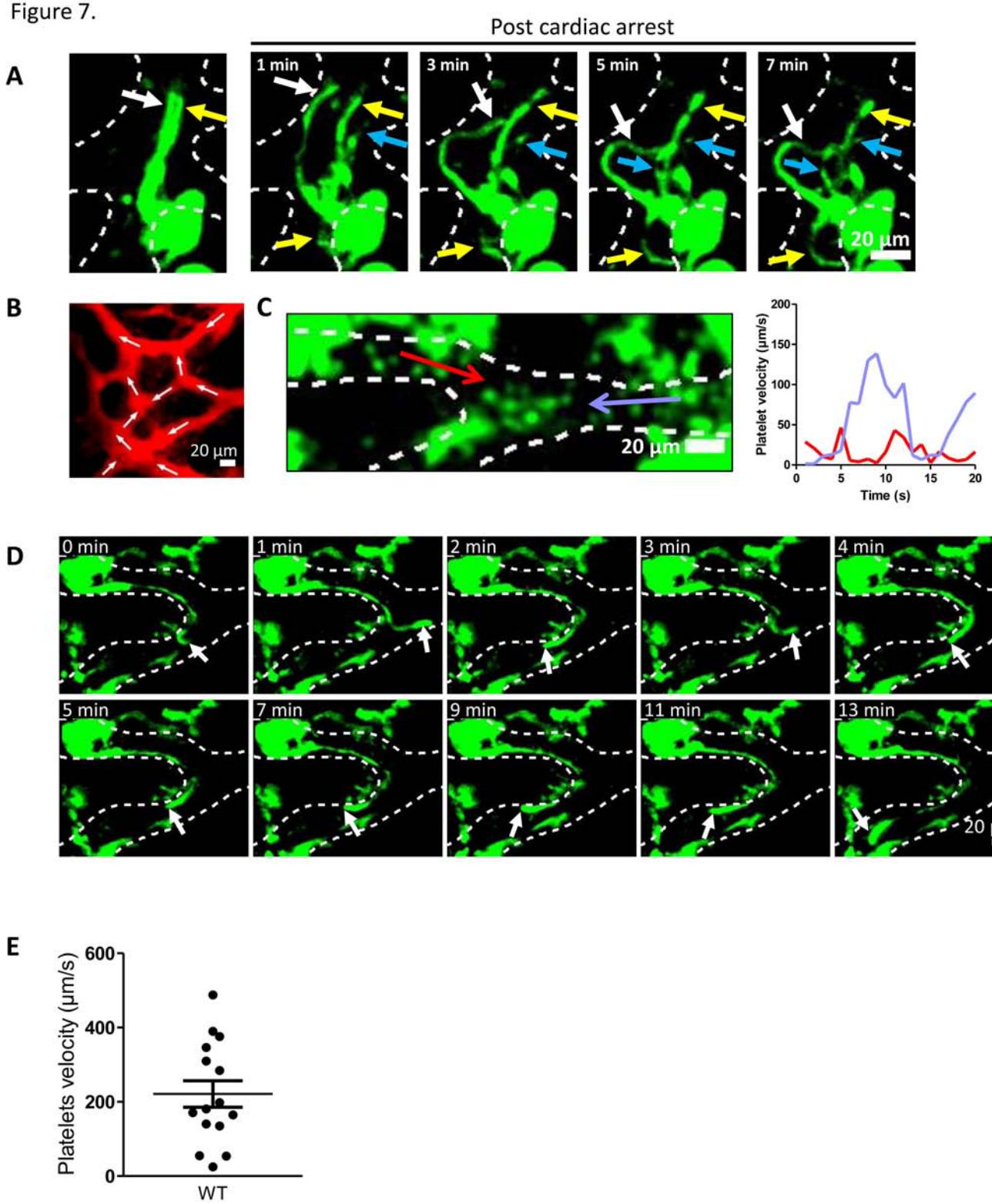
Post cardiac arrest
A
1 min
3 min
5 min
7 min
20 µm
B
20 µm
C
20 µm
Platelet velocity (µm/s)
200
150
100
50
0
0
5
10
15
20
Time (s)
D
0 min
1 min
2 min
3 min
4 min
5 min
7 min
9 min
11 min
13 min
20 µm
E
Platelets velocity (µm/s)
600
400
200
0
WT

Figure 8.

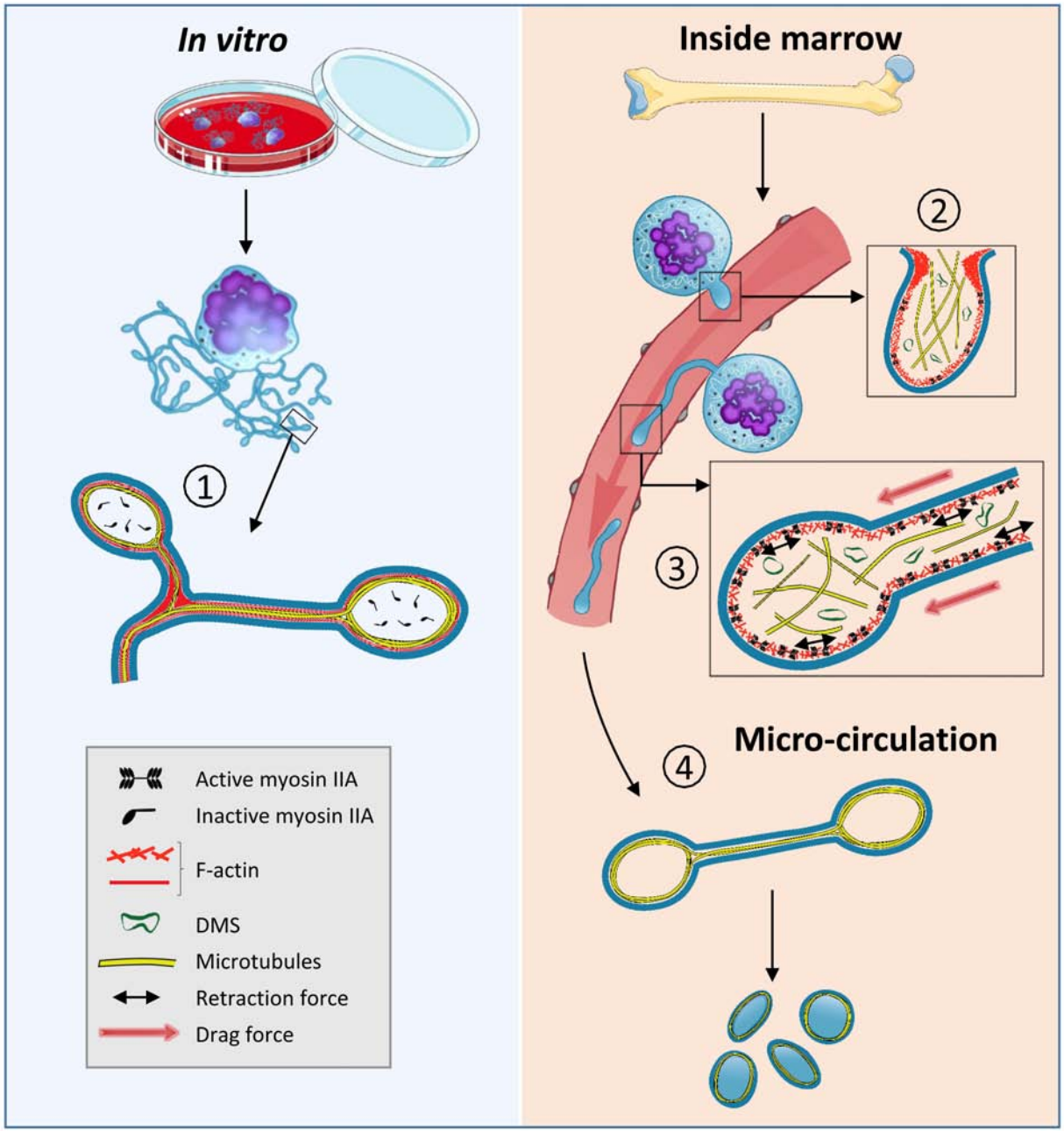
In vitro
Inside marrow
1
2
3
4
Micro-circulation
Active myosin IIA
Inactive myosin IIA
F-actin
DMS
Microtubules
Retraction force
Drag force

Supplemental Data

Cytoskeletal-based mechanisms differently regulate *in vivo* and *in vitro* proplatelet formation

Alicia Bornert[1], Julie Boscher[1], Fabien Pertuy[1], Anita Eckly[1], David Stegner[2], Catherine Strassel[1], Christian Gachet[1], François Lanza[1], Catherine Léon[1*]

Supplemental Materials and Methods.

Materials

Vascular Labels Qtracker™ 655, DAPI and ProLong Gold were purchased from Invitrogen (Eugene, OR, USA). Vincristine and bovine serum albumin (BSA) were from Sigma-Aldrich (Rueil-Malmaison, France). The Alexa Fluor 488-labeled anti-GPIX antibody derivatives were kindly provided by Prof. Dr. Bernhard Nieswandt (Institute of Experimental Biomedicine, University Hospital Würzburg, Germany)[52]. The anti-GPIbβ antibody (RAM1) was produced in our laboratory and the AF488-labeled anti-α tubulin antibody was from Invitrogen (clone DM1A). Histoacryl surgical glue was from Braun Surgical (Rubí, Spain). Dental paste (Picodent twinsil speed) was from Picodent (Wipperfürth, Germany).

Mice

Male and female mice between 5 and 7 weeks old were used for intravital imaging. *mT/mG;Pf4-cre* mice were generated by crossing B6.129(Cg)-*Gt(ROSA)26Sor*$^{tm4(ACTB-tdTomato,-EGFP)Luo}$/J with *Pf4-cre* mice to obtain eGFP expression in MKs and platelets, as described previously[53]. Mice deficient in myosin IIA (*Myh9*$^{-/-}$ mice)[54], mice lacking β1 tubulin (*Tubb1*$^{-/-}$ mice)[28] and control mice had a C57BL/6J genetic background. Animal experiments were performed in accordance with European law and the recommendations of the Review Board of the Etablissement Français du Sang (EFS) and the Institut de

Génétique et de Biologie Moléculaire et Cellulaire (IGBMC) regarding animal care and agreement for experimentation obtained from the French government.

Intravital imaging

Mice were anesthetized by injection of a solution of ketamine (100 µg/g) and xylazine (10 µg/g). The scalp was incised at the midline to expose the calvarium and the periosteum was removed without damaging the bone. A 3D printed ring was glued to the mouse skull using surgical glue and silicone dental paste was deposited around the ring to prevent leakage. The ring was filled with physiological saline to keep the skull wet and serve as an immersion medium for the microscope objective. The mouse was placed on a temperature-controlled plate at 37°C during surgery and kept for a maximum of 3h under the microscope inside an environmental chamber at 37°C, in agreement with the local ethical and animal welfare comity. Although the visualized events are relatively rare, this time was sufficient to record elongation from already extended nPPTs. The anesthesia was re-induced every 35 min by alternating subcutaneous injections of ketamine (25 µg/g) and a mixture of ketamine (50 µg/g) and xylazine (5 µg/g). To characterize PPTs, we used *mT/mG;Pf4-cre* whose MKs express the fluorescent reporter protein. To evaluate nPPT formation in knockout animals, MKs and platelets were stained by intravenous injection of an AF488-conjugated anti-GPIX antibody derivative[52]. Of note, nPPTs exhibited identical morphologies whether they were observed from mT/mG;Pf4-cre mice or mice injected with the antibody (Suppl. Fig. S1C shows the measured nPPT width for both mouse models). The BM vasculature was visualized by intravenous injection of Qtracker 655. In some mice, vincristine (100 µL) was administered at a dose of 1 or 2 mg/kg to give respectively a final concentration of about 10 or 20 µg/mL (≈ 10 or 20 µM) in the circulating blood, assuming a total blood volume of 2 mL/mouse.

Two-photon microscopy

Intravital imaging was performed using a Leica SP8 confocal microscope equipped with a 25x water objective with a numerical aperture of 0.95 (Leica) (IGBMC/CBI plateform, Illkirch) or a Leica MP

DIVE (EFS, Strasbourg). A femtosecond Ti:Saph pulsing laser (Coherent) was used at 913 nm to simultaneously excite AlexaFluor-488 and Qtracker-655. The emitted light was detected using non-descanned HyD hybrid detectors with 525/25 and 617/73 filters. Images were recorded with a resonant scanner (12 kHz for the SP8, 8 kHz for the MP DIVE) in bidirectional mode and an adapted averaging.

Acquisition and analysis of nPPT images

To study PPT formation, the x-y surface area (384 x 384 pixels) was visualized at 10 s intervals and z-stack images were acquired with z-depths of 1.34 µm. All images were analyzed with ImageJ software (National Institute of Health, Bethesda, MD). The profiles were aligned if necessary using the ImageJ template matching plug-in and an average z-projection was obtained. Depending on the image quality, the background was subtracted, the image was smoothed and the brightness and contrast adjusted. To measure the width of nPPT, a perpendicular line was drawn at a fixed position close to the base of the nPPT and the profile intensity was recorded at this position every minute (see Suppl. Fig. S1A). A Gaussian curve was fitted to this profile and the FWHM (Full Width at Half Maximum) was considered to represent the width of the nPPT. The mean width was then calculated by averaging the widths of the nPPT measured at each time point at the fixed position. The maximal nPPT length was also determined, from the base of the nPPT to its tip. The net mean nPPT elongation speed (including pause and retraction) was calculated as the change in nPPT length at one minute intervals and averaged over the whole time sequence. To better highlight the pauses and retractions upon the process of nPPT growth, the length measured every 10 sec was represented as a percentage of the maximal length of each individual nPPT, mentioned in the Figure legend. For the vincristine experiments, the length and width measurements were done once immediately before drug administration and other measurements were performed every minutes, from 0.5 min after vincristine injection to up to 15 min for some PPTs. Measurements of cPPTs were performed on phase contrast imaged from cPPT extended in the explant model. The same method as above was used, except for the bud width where a threshold was applied before measurements.

Measurement of Blood flow

Blood flow was estimated by measuring the displacement of circulating platelets within a small x-y area (256 x 90 pixels) to maximize the frame acquisition rate. A maximum of 133 frames/s could be obtained and displacement were usually acquired during 20 seconds. The blood flow in a portion of a vessel was determined using ImageJ line-scan software at three different positions, i.e. in the center and close to opposite vessel walls. The resulting images represent the successive linear scans stacked over time. These space-time images shows the moving platelets, as diagonal streaks, where the slope is related to their velocity. The images were then exported into GNU Octave software to determine the flow velocity using the Radon transform method[55].

***In vitro* proplatelet formation.**

For explant bone marrow experiments, marrows were flushed out of mouse femurs and cut into transverse sections of 0.5 mm-thick. Megakaryocytes were observed after 6 h of incubation at 37°C, at the periphery of the tissue, as described[26].

In vitro liquid culture of Lin^- mouse progenitors was performed as described previously[56]. Bone marrow cells were flushed from femurs and tibias from 8- to 12-week old male C57Bl/6 mice and successively passed through 21-, 23- and 25-gauge needles. The cells were spun down and nucleated cells were counted. Cells were pelleted at 300g for 7 min and resuspended at 1×10^8 cells/ml in PBS supplemented with 2% (v/v) FBS and 2 mM EDTA to perform the lineage (Lin) negative selection, according to the recommendations of the manufacturer (Stem Cell Technologies). The Lin^- population was adjusted to 2×10^6 cells/mL in DMEM containing 2 mM glutamine, penicillin/streptomycin, 10% FBS, 50 ng/mL TPO and 100 U/mL hirudin (complete medium). Cultures were performed in 24-well tissue culture plates using 500 µL of cell suspension in liquid medium per well and were incubated at 37 °C under a 5% CO_2 atmosphere. MKs extended PPTs after 4 days culture.

Immunofluorescence and confocal observations

For *in situ* immunolabeling of bone marrow, we took care to preserve the cytoskeleton. For that, we first injected 200 µL/20g mouse of a 5 mM Paclitaxel solution intravenously (i.v.) into anesthetized mice. After 3 min a second i.v. injection of 300 µL PFA 12% was performed, femurs were immediately removed and the marrow was flushed directly into the fixative solution (4% PFA in PHEM buffer containing 50 µM Paclitaxel and 100 nM phalloidin). After fixation for 24 h and cryopreservation in sucrose, the marrow was embedded in freezing medium and cryosections 30 µm were cut. Immunolabeling on thick marrow sections was performed by O/N incubation with AF-488 labeled anti-α tubulin antibody (10 µg/mL), 1-h washes and incubation with AF-555 labeled anti-GPIbβ antibody (10 µg/mL) for 1 more hour, then mounting in ProLong Gold.

For platelet labeling, blood was drawn from the abdominal aorta of anesthetized mice and 0.38% citrated platelet rich plasma (cPRP) was prepared by blood centrifugation (10 min, 250g), then fixed in 4% PFA and cytospun. For cPPT labeling, 4-days cultured MKs were fixed in 4% PFA and cytospun. Immunolabeling was done using the same antibodies and protocol as described above for *in situ*, except for anti-tubulin antibody which was incubated only for 1 h.

Images were acquired using a Leica SP8 inverted confocal microscope, equipped with a 63x oil immersion objective (1.4 NA) and Leica Application Suite software (LASX). Images are either a single z-plane, or a z-stack and 3D reconstruction (Fig. 1Ai-ii and 4C). The presented images are the raw images without any post-treatment except for Fig. 4B and C where a deconvolution treatment was applied using Huygens software. The proportion of PPT fragments from WT and *Tubb1*$^{-/-}$ was quantified by performing z-stack acquisitions (dimension of the acquisition field 400 x 400 x 30 µm). A 3D reconstruction using LASX and observations in all directions allowed to visualized MKs and PPT fragments. We considered a PPT fragment any GPIbβ-positive element having a rod-like shape longer than 15 µm.

Scanning electron microscopy.

To visualize the intracellular cytoskeletal filaments, cultured megakaryocytes were incubated for 5 min with 0.5% Triton X-100 in PHEM containing 0.1% glutaraldehyde, 5 μM phalloidin and 30 μM taxol. The resulting cytoskeletons were fixed in 1% glutaraldehyde for 10 min and allowed to adhere by sedimentation to the surface of poly-L-lysine-coated coverslips. After three washes in PBS and dehydration in graded ethanol solutions, the samples were air-dried with hexamethyldisilazane, sputtered with gold and examined under a scanning electron microscope (Sirion, FEI, The Netherlands). For cPPT, samples were fixed with 2.5% glutaraldehyde in 0.1 M cacodylate buffer (pH 7.2) and prepared for SEM observation as above, without the detergent step. For the *in situ* marrow nPPT visualization, the dehydrated whole marrow fragment was further fragmented.

Statistics.

Data are presented as mean ± standard error of mean (sem). Comparison between 2 groups were performed using two-tailed Student's t-test or Mann-Whitney test when number was too small or when the population did not pass the normality test, mentioned in figure legends.*, $p<0.05$; **, $p<0.01$; ***, $p<0.0001$; ns, $p>0.05$

Legends to Supplemental Figures and videos

Supplemental Figure S1. Morphological characteristics of *in vivo* PPTs. A) Upper, z-projection image depicting the site where the nPPT width was measured together with maximal length. Middle, maximal length of 25 individual nPPTs obtained from 14 mice. The same color has been attributed to nPPT observed in the same mouse. Bottom, mean nPPT width measured at the base of the nPPT over the course of elongation for 28 individual nPPTs obtained from 19 mice. Bars are mean±sem of the width measured every minutes during acquisition. The same color has been attributed to nPPT observed in the same mouse. B) Time lapse showing nPPT detaching from its base. C) Mean nPPT width showing no difference between mTmG/Pf4-cre mice (15 nPPTs pooled from 10 mice) and WT mice injected with the anti-GPIX antibody (13 nPPTs pooled from 9 mice) (ns, not significant with unpaired Student't t-test).

Supplemental Figure S2. Presence of pauses and retractions in WT mice while absence in *Myh9*$^{-/-}$ mice. A) Scatter plot representing the nPPT elongation speed calculated in WT mice. Individual values and mean ± sem. Data are 12 nPPTs pooled from 8 mice. B-C) Individual tracings showing the elongation behavior of WT (B) and *Myh9*$^{-/-}$ (C) nPPT, some of the WT nPPT presenting pause and retraction phases while they are absent during the course of *Myh9*$^{-/-}$ nPPT elongation. Data presented as the % of maximal nPPT length. Data are 11 nPPTs pooled from 10 WT mice and 6 nPPTs pooled from 4 *Myh9*$^{-/-}$ mice.

Supplemental Figure S3. Decreased PPT fragments and platelet count in *Tubb1-/-* mice but normal granule distribution. A) 3D view rendering of 30 µm-thick WT or *Tubb1*$^{-/-}$ marrow sections

acquired by confocal microscopy, immunolabeled for GPIbβ to visualize MKs and platelets (magenta). Arrows show nPPTs or nPPT fragments longer than 15 µm. Note the higher number of MKs in the *Tubb1*$^{-/-}$ marrow. B) Left, quantification of platelet counts in circulating blood of 18-days or 8-weeks old WT *vs*. *Tubb1*$^{-/-}$ mice. Right, Mean platelet volume for the same mice. ***, p<0.0001 using two-tailed unpaired Student's t-test. n=6 mice. C) TEM images showing platelet ultrastructure from WT and *Tubb1-/-* mice. Representative of 2 independent platelet preparations.

Supplemental Figure S4. Impact of vincristine on WT and *Myh9*$^{-/-}$ *platelet* marginal band, *in vitro* and *in vivo*. A) Vincristine (20 µM) was added to fresh WT or *Myh9*$^{-/-}$ cPRP for the indicated time. PRP was PFA-fixed and cytospun before immunolabeling with anti-α tubulin antibody. Images are representative of 2 experiments and were acquired by confocal microscopy. Bar is 30 µm. B) Vincristing (2 mg/kg) was administered i.v. in WT or *Myh9-/-* mice for the indicated time and blood was drawn using citrate 0.38% final concentration as an anticoagulant. cPRP was prepared and fixed within less than 1.5 minutes from blood drawing. Microtubules are visualized by immunolabeling with anti-α tubulin antibody. Images representative of 3 independent experiments.

Supplemental Figure S5. *In situ* observation of microtubules and F-actin following vincristine administration.

Confocal plane images showing MK from untreated mice (left images) or from mouse injected with vincristine (1 mg/kg) (right images) for 10 minutes. A) WT mice, and B) *Myh9*$^{-/-}$ mice, top panels are GPIbα labelings, middle panels are α-tubulin labelings, and bottom panels are F-actin labelings (phalloidin). Representative of at least 3 sections from 2 mouse marrows.

Supplemental Figure S6. Impact of vincristine 1mg/kg injection on native PPT length. A) Measurement of nPPT length in *Myh9*$^{-/-}$ mice before and after 1 mg/kg vincristine administration plotted as a function of time. Seven *Myh9*$^{-/-}$ mice analyzed. B) Measurement of the difference in nPPT length

during a 10-min window post-vincristine administration (1 mg/kg), showing decreasing length in WT (n=7) (left) while increasing length despite vincristine injection in *Myh9*$^{-/-}$ mouse nPPT (n=4) (right).

Supplemental Figure S7. *In situ* observation of nPPT from *Myh9*$^{-/-}$ marrow.

Confocal image showing microtubules (AF-488 α-tubulin labeling) and F-actin (AF-647 phalloidin labeling) in a *Myh9*$^{-/-}$ PPT, visualized by anti-GPIbα labeling. Image to be compared to the WT one in Fig. 4D and E.

Supplemental Figure S8. *Myh9*$^{-/-}$ nPPT are poorly enriched in DMS. TEM images showing nPPT observed in *in situ* bone marrow sinusoids from either WT or *Myh9*$^{-/-}$ mice. Red arrows denote nPPT fragments. s, sinusoid; e, erythrocyte. Observations from 2 WT and 2 *Myh9*$^{-/-}$ mice.

Video 1: Representative time lapse video (z-projection) recording WT mouse with MK extending an elongating nPPT (green) within bone marrow sinusoids (red, Qtracker).

Video 2: Representative time lapse video (z-projection) recording WT mouse, showing a MK extending a short and large nPPT (arrow) and another MK extending a long, thin, regular and rapidly growing nPPT in the right vessel. nPPTs (green) within BM sinusoids (red, Qtracker).

Video 3: Representative time lapse video (z-projection) recording WT mouse with MK extending a very long nPPT. nPPT (green) within BM sinusoids (red, Qtracker) is shown.

Video 4: Effect of vincristine on WT PPT *in vivo*. Time lapse video recording an nPPT in WT mouse before and after administration of vincristine (1 mg/kg) (z-projection). The elongating nPPT (green) within the sinusoid vessels (red) starts to retract after intravenous administration of vincristine.

Video 5: Effect of vincristine on *Myh9*$^{-/-}$ PPT *in vivo*. Time lapse video recording of MK protrusion in *Myh9*$^{-/-}$ mouse before and after administration of vincristine (1 mg/kg) (z-projection). The elongating nPPT (green) within the sinusoid vessels (red) continue to elongate despite vincristine administration.

Video 6: Impact of mouse cardiac arrest in PPT morphology. Time lapse video recording ofn in a *Myh9*$^{-/-}$ mouse before and after cardiac arrest. The video shows 3 nPPTs (green, labeled with AF-488 anti-GPIX antibody derivative) in the same flow line before cardiac arrest, thus not individualized at the resolution of the two-photon microscopy. Following cardiac arrest, the 3 nPPTs separate and become relaxed in the absence of blood flow, but without retracting.

Video 7: Reverse flow within sinusoid. Circulating platelets (green) within the sinusoid vessels (red, Qtracker) (single confocal z-plane). An anastomosed sinusoid vessel is shown presenting bifurcations where the flow is unstable and displays phases of stasis, accelerations and decelerations.

Video 8. nPPT tossed by the reverse flows. Time lapse video showing a WT MK in the sinusoid bifurcation shown in video 4, in the process of extending an nPPT that oscillate in one vessel branch depending on the direction of flow (z-projection).

Supplemental Figure S1. Morphological characteristic of *in vivo* nPPTs

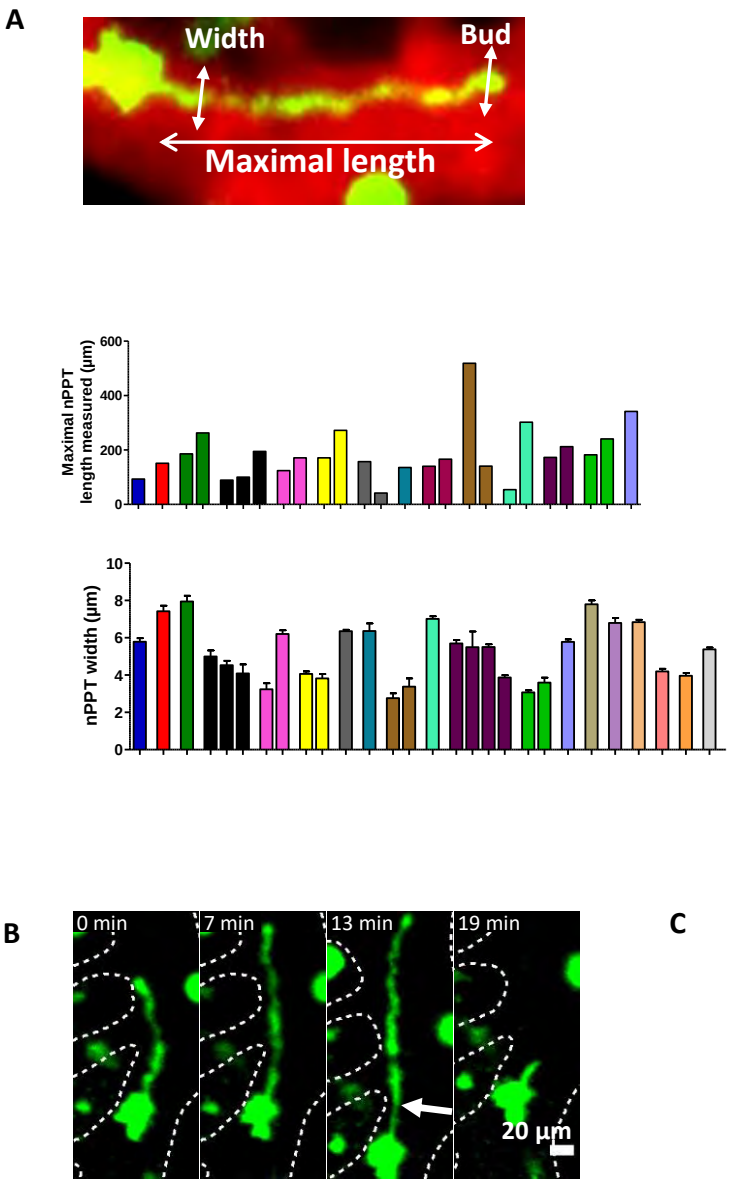

Supplemental Figure S2. Presence of pauses and retractions in WT mice while absence in *Myh9*$^{-/-}$ mice.

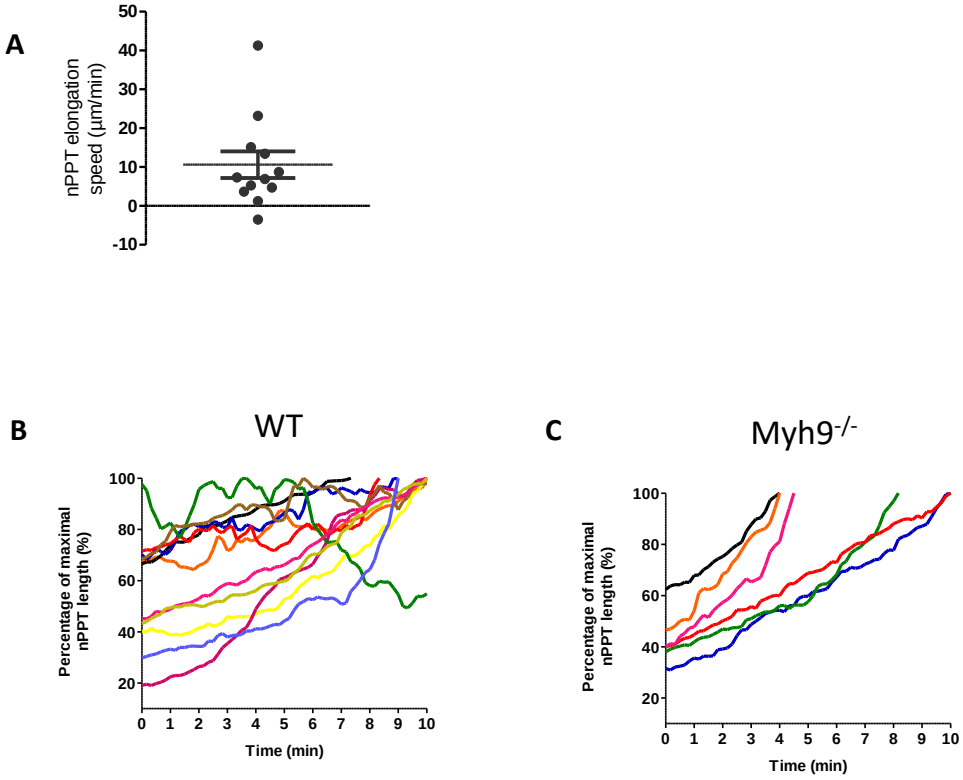

Supplemental Figure S3. Decreased nPPT fragments and platelet count in Tubb1-/- mice but normal granule distribution.

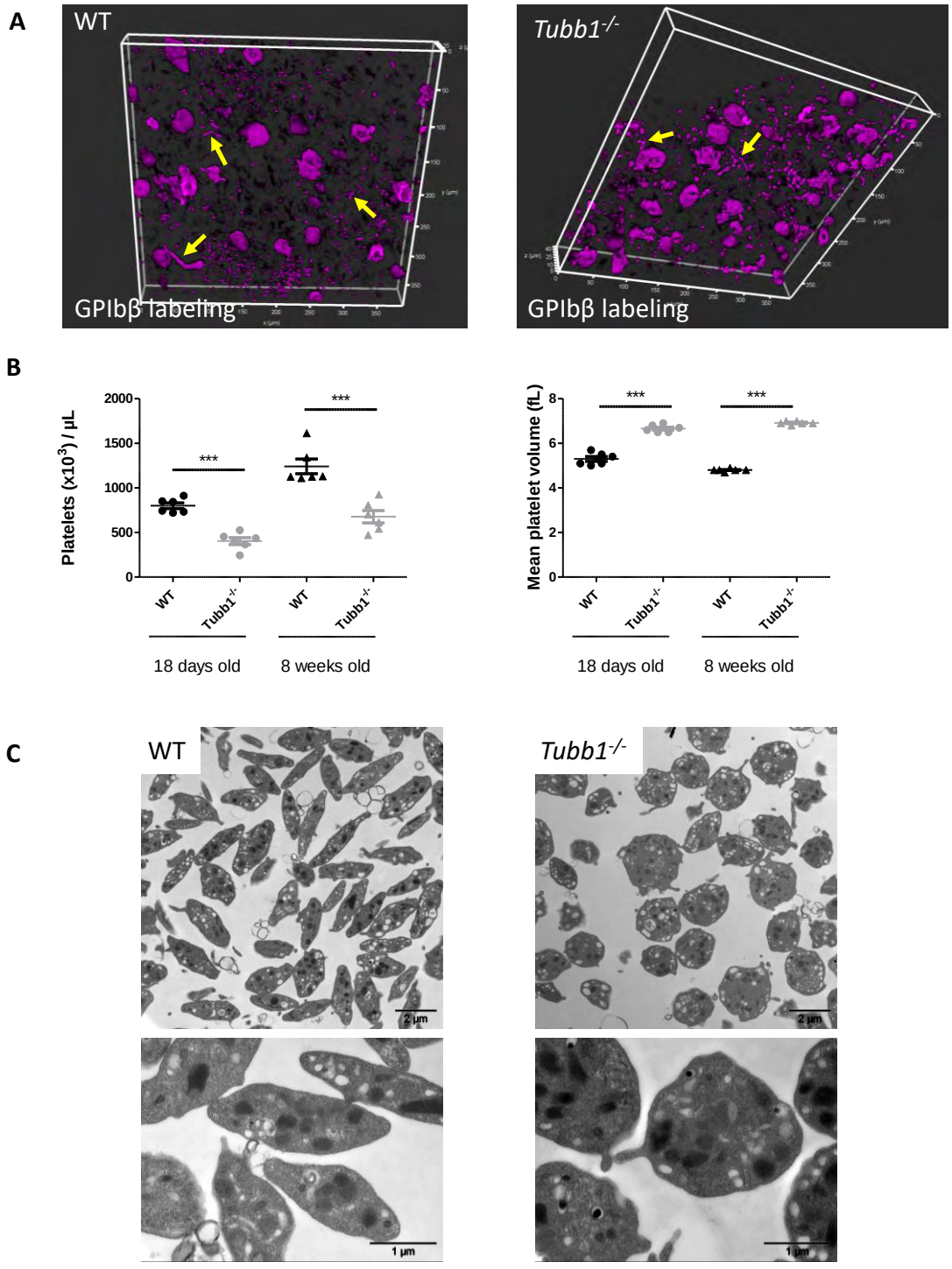

Supplemental Figure S4. Impact of vincristine on WT and *Myh9*$^{-/-}$ platelet marginal band, *in vitro* and *in vivo*

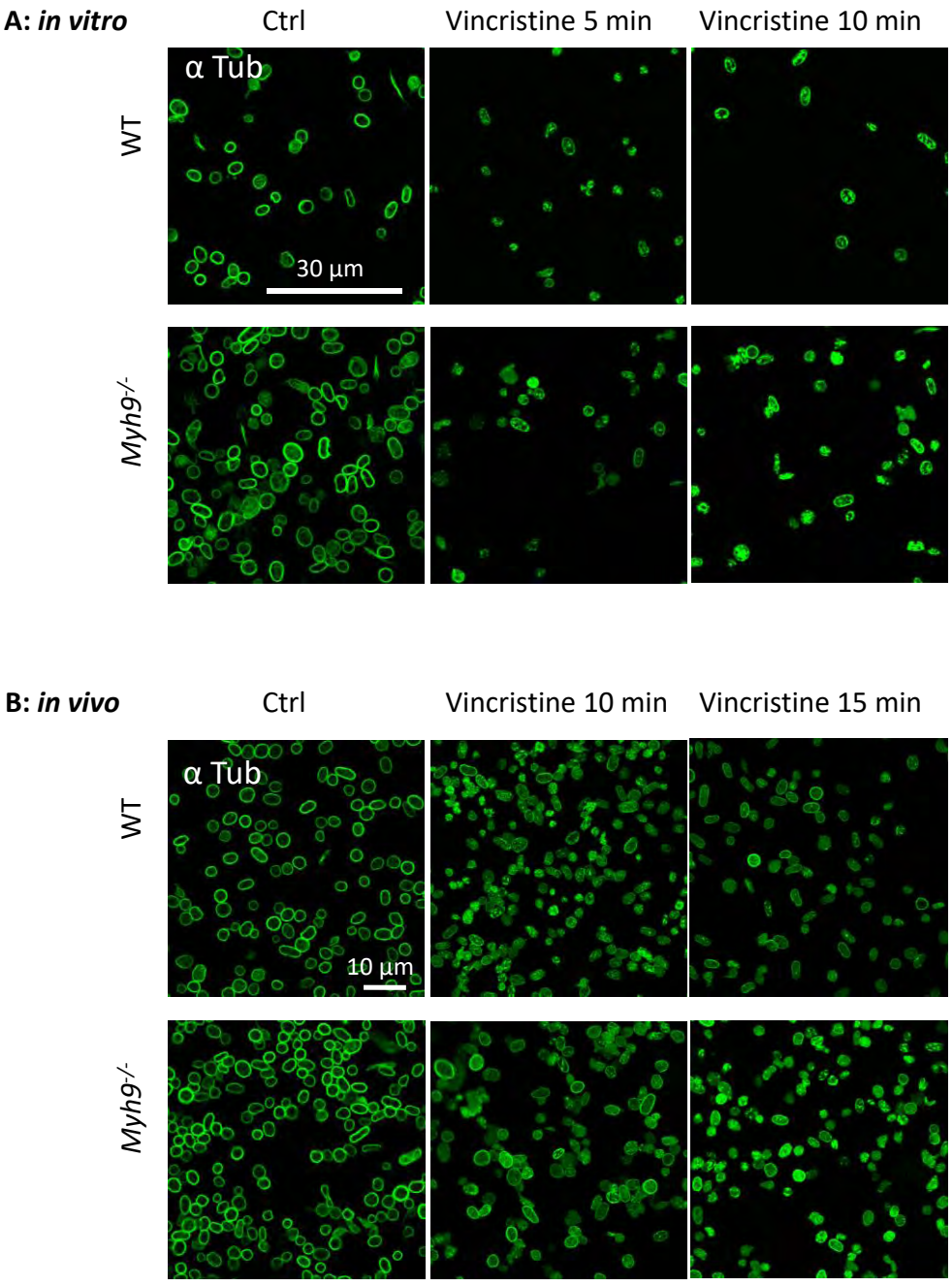

Supplemental Figure S5. *In situ* observation of microtubules and F-actin following vincristine administration.

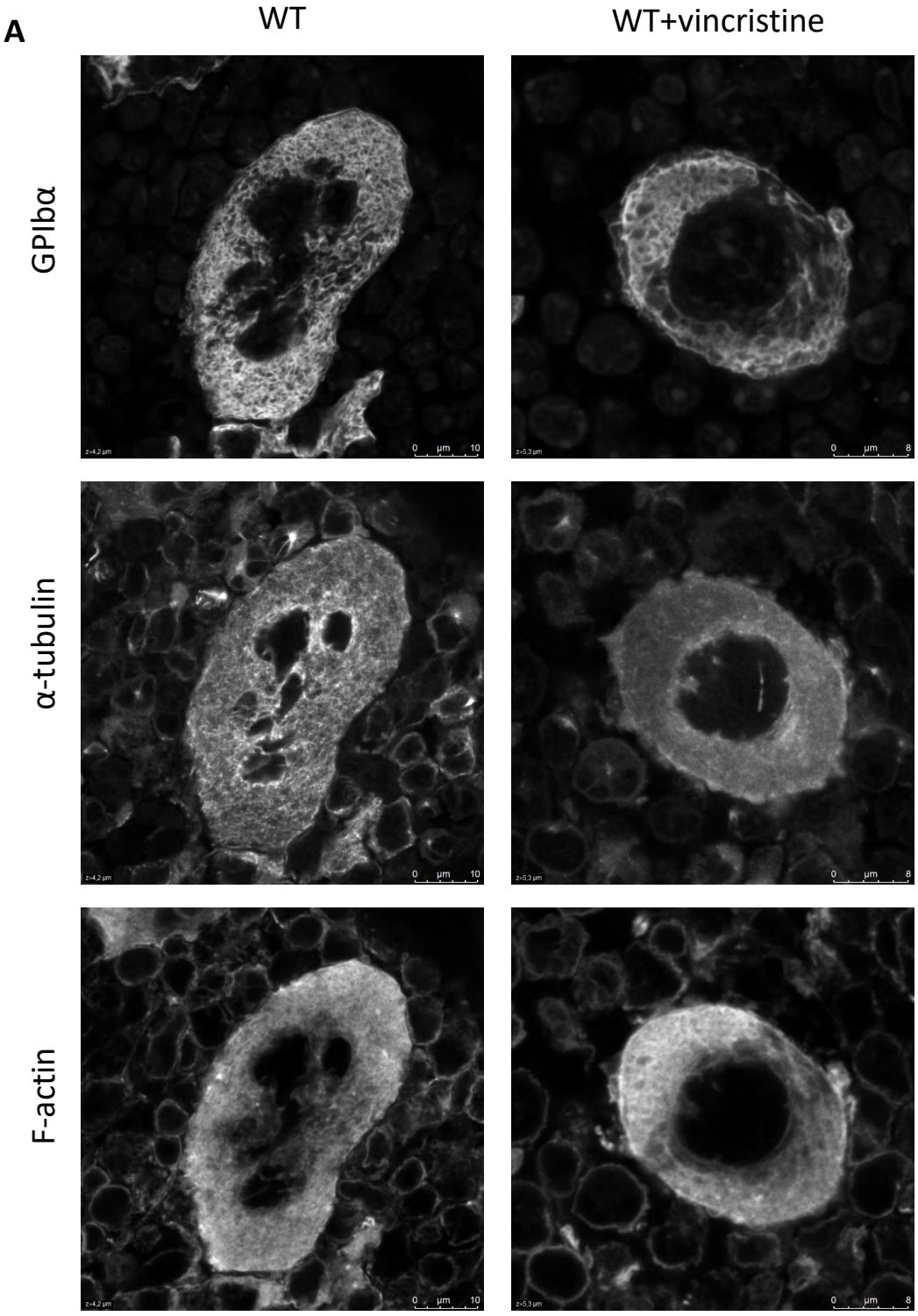

Supplemental Figure S5. *In situ* observation of microtubules and F-actin following vincristine administration.

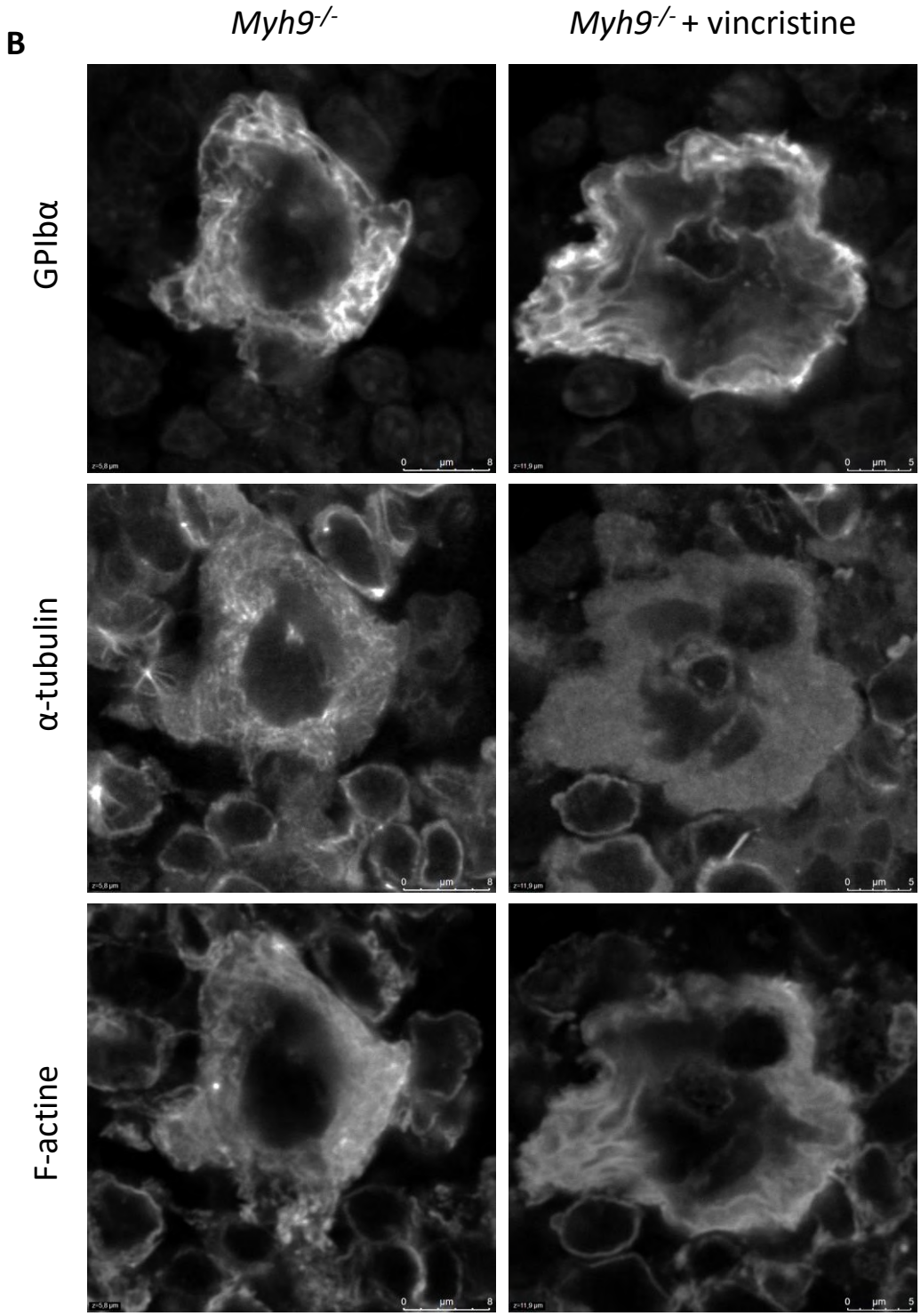

Supplemental Figure S6. Impact of vincristine 1mg/kg injection on nPPT length.

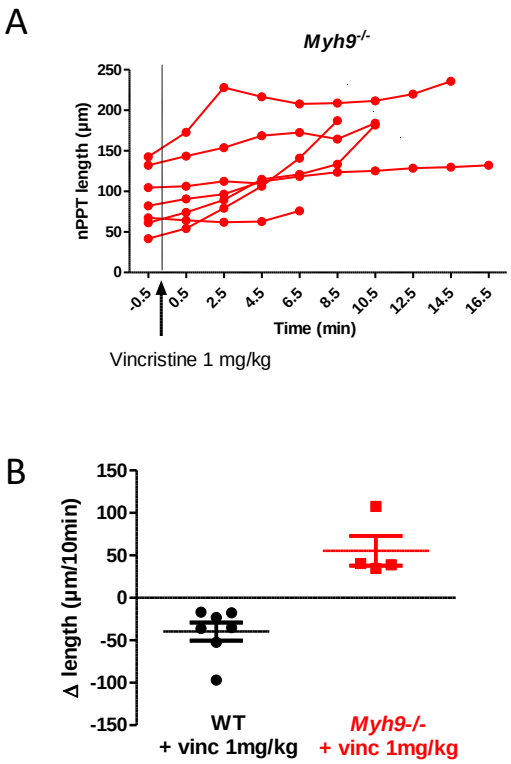

Supplemental Figure S7. *In situ* observation of nPPT from *Myh9*$^{-/-}$ marrow.

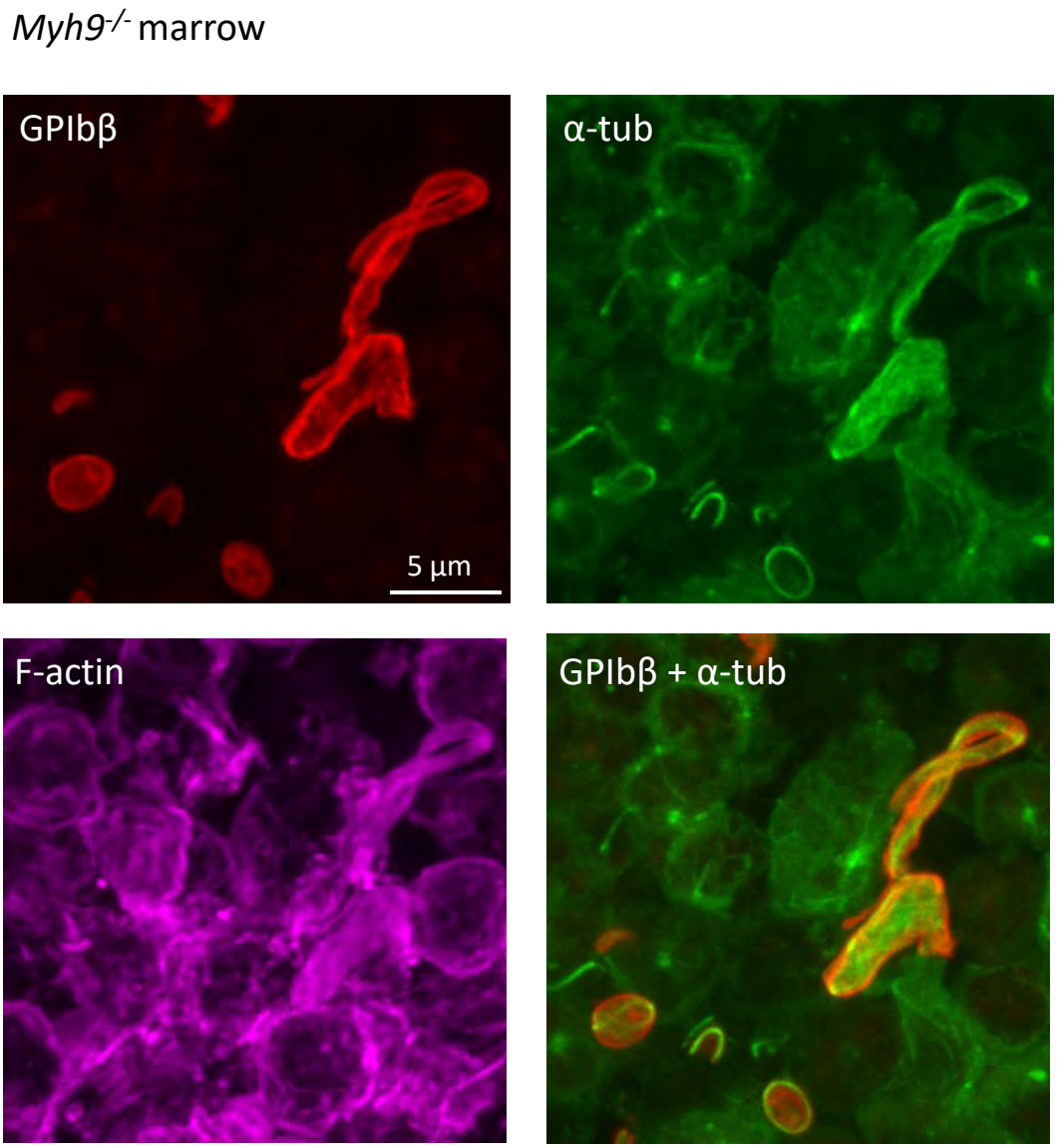

Supplemental Figure S8. *Myh9*$^{-/-}$ nPPT are poorly enriched in DMS.